


Magnetohydrodynamic simulation code CANS+: Assessments and applications

Yosuke MATSUMOTO ^{1,2,*} Yuta ASAHINA,³ Yuki KUDOH,⁴
Tomohisa KAWASHIMA,^{5,6} Jin MATSUMOTO,⁷ Hiroyuki R. TAKAHASHI,^{8,9}
Takashi MINOSHIMA,¹⁰ Seiji ZENITANI,^{11,12} Takahiro MIYOSHI,¹³
and Ryoji MATSUMOTO¹

¹Department of Physics, Graduate School of Science, Chiba University, 1-33 Yayoi-cho, Inage-ku, Chiba 263-8522, Japan

²Institute for Global Prominent Research, Chiba University, 1-33 Yayoi-cho, Inage-ku, Chiba 263-8522, Japan

³Center for Computational Sciences, Tsukuba University, 1-1-1 Tennodai Tsukuba-city, Ibaraki 305-8577, Japan

⁴Graduate School of Science and Engineering, Kagoshima University, Korimoto 1-21-24, Kagoshima, Kagoshima 890-0065, Japan

⁵Center for Computational Astrophysics, National Astronomical Observatory of Japan, 2-21-1 Osawa, Mitaka, Tokyo 181-8588, Japan

⁶Division of Theoretical Astronomy, National Astronomical Observatory of Japan, 2-21-1 Osawa, Mitaka, Tokyo 181-8588, Japan

⁷Research Institute of Stellar Explosive Phenomena, Fukuoka University, 8-19-1 Nanakuma, Jonan-ku, Fukuoka, Fukuoka 814-0180, Japan

⁸Engineering Science Laboratory, Chubu University, 1200 Matsumoto-cho, Kasugai, Aichi 487-8501, Japan

⁹Faculty of Arts and Sciences, Department of Natural Sciences, Komazawa University, 1-23-1 Komazawa, Setagaya-ku, Tokyo 154-8525, Japan

¹⁰Center for Mathematical Science and Advanced Technology, Japan Agency for Marine-Earth Science and Technology, 3173-25 Syowa-machi, Kanazawaku, Yokohama, Kanagawa 236-0001, Japan

¹¹Research Institute for Sustainable Humanosphere, Kyoto University, Gokasho, Uji, Kyoto, Kyoto 611-0011, Japan

¹²Research Center for Urban Safety and Security, Kobe University, 1-1 Rokkodai-cho, Nada-ku, Kobe, Hyogo 657-8501, Japan

¹³Graduate School of Science, Hiroshima University, 1-3-1 Kagamiyama, Higashi Hiroshima, Hiroshima 739-8526, Japan

*E-mail: [ymatumot@chiba-u.jp](mailto:yumatmot@chiba-u.jp)

Received 2019 March 15; Accepted 2019 May 13

Abstract

We present a new magnetohydrodynamic (MHD) simulation package with the aim of providing accurate numerical solutions to astrophysical phenomena where discontinuities, shock waves, and turbulence are inherently important. The code implements the Harten–Lax–van Leer–discontinuities (HLLD) approximate Riemann solver, the fifth-order-monotonicity-preserving interpolation (MP5) scheme, and the hyperbolic divergence cleaning method for a magnetic field. This choice of schemes has significantly

improved numerical accuracy and stability, and saved computational costs in multidimensional problems. Numerical tests of one- and two-dimensional problems show the advantages of using the high-order scheme by comparing with results from a standard second-order total variation diminishing monotonic upwind scheme for conservation laws (MUSCL) scheme. The present code enables us to explore the long-term evolution of a three-dimensional accretion disk around a black hole, in which compressible MHD turbulence causes continuous mass accretion via nonlinear growth of the magnetorotational instability (MRI). Numerical tests with various computational cell sizes exhibits a convergent picture of the early nonlinear growth of the MRI in a global model, and indicates that the MP5 scheme has more than twice the resolution of the MUSCL scheme in practical applications.

Key words: magnetohydrodynamics (MHD) — methods: numerical — shock waves — turbulence

1 Introduction

In recent decades, computational astrophysics has emerged together with a rapid growth of computational capabilities, enabling us to reveal various aspects of astrophysical phenomena that cannot be provided by observations. Among them, magnetohydrodynamic (MHD) simulations are powerful tools for understanding space and astrophysical phenomena such as solar flares and coronal mass ejections, auroral substorms in the terrestrial magnetosphere, magnetic dynamos in accretion disks and associated jet accelerations. In most cases, the systems are dominated by various MHD discontinuities, shock waves, and turbulence in which the fluid dynamics are strongly coupled with the magnetic field. Such highly nonlinear systems have stimulated the search for numerical algorithms that can solve the MHD equations with both high accuracy and stability.

Early development of MHD simulation code was based on finite difference schemes with artificial and/or numerical dissipation, such as the modified Lax–Wendroff scheme (Rubin & Burstein 1967; Shibata 1983). The high-order upwind scheme was implemented in the ZEUS code (Stone et al. 1992; Hawley & Stone 1995) and has been used for many applications in astrophysics owing to its simplicity and flexibility. However, besides these early successes in computational astrophysics, overcoming spurious (grid) oscillations in highly stratified, compressible MHD applications has remained a task for further improvement in the numerical schemes (e.g., Kudoh et al. 1999).

Modern MHD simulation codes have a strategy of accurately capturing shock waves as they often accompany supersonic flows in space and astrophysical phenomena. Such shock-capturing schemes are based on the finite volume method in which the time evolution of cell-averaged conservative variables of the MHD equations is calculated from numerical fluxes at the cell surfaces. Thus, the accuracy and the robustness rely on the method of obtaining the numerical flux from the cell-averaged conservative variables.

In the numerical flux calculation, upwind natures are incorporated by solving a Riemann problem at the cell interface initiated with the two neighboring cell states. The so-called Godunov schemes are based on the idea that the numerical flux can be obtained by integrating the conservative variables in the Riemann fan following conservation laws in space and time. Various approximate Riemann solvers have been developed for numerical solutions to the Riemann problem, including Roe’s scheme (Roe 1981) and a family of Harten–Lax–van Leer (HLL) solvers (Harten et al. 1983; Li 2005; Miyoshi & Kusano 2005). Among them, the HLLD (where D stands for discontinuities) approximate Riemann solver of Miyoshi and Kusano (2005) is now the standard method in modern MHD codes (see, e.g., Kritsuk et al. 2011) as it provides tractable and stable numerical solutions.

Special care must be taken in multidimensional MHD simulations as the solenoidal property of the magnetic field cannot be straightforwardly satisfied, and numerical errors from the divergence-free condition severely affect results, in particular when solving the conservative forms of the MHD equations numerically. While divergence cleaning methods aim to maintain the numerical errors within minimal levels by making modifications to the base equations (Brackbill & Barnes 1980; Powell et al. 1999; Dedner et al. 2002), the constrained-transport (CT) algorithm (Evans & Hawley 1988) accomplishes the divergence-free condition within the level of machine round-off errors by adopting a special discretization for the magnetic field. Nowadays, most MHD codes employ variants of the CT algorithm while preserving the upwind nature for the induction equation of the magnetic field (Londrillo & Del Zanna 2004; Gardiner & Stone 2005; Lee & Deane 2009; Miyoshi & Kusano 2011; Minoshima et al. 2015, 2019; Lee et al. 2017). For further information, readers may consult comprehensive comparisons of the schemes by Tóth (2000), and also, for more recent schemes, by Miyoshi and Kusano (2011).

Extensions of the scheme to a higher-order accuracy have been accomplished by adopting piecewise high-order polynomials to reconstruct variables' profiles in each cell used for the local Riemann problem at the cell interface, with which the total variation diminishing (TVD) property has been necessarily incorporated by adopting various slope limiters, so that the profiles degrade to the first order around discontinuities. The so-called monotonic upwind scheme for conservation laws (MUSCL) scheme (van Leer 1979) and its extension of the third-order piecewise parabolic method (PPM) scheme (Colella & Woodward 1984) have been widely implemented for practical use in public MHD codes such as FLASH (Lee & Deane 2009; Lee 2013), PLUTO (Mignone et al. 2007), and Athena (Stone et al. 2008); see also Kritsuk et al. (2011) for other MHD codes. Note, however, that the overall spatial accuracy of such CT-based MHD code has been achieved only up to the second order because the original CT algorithm is based on a second-order discretization. A third-order scheme has been proposed in the framework of upwind CT (UCT), with additional large computational costs arising from high-order reconstructions and solutions of the Riemann problem at the cell edge (Londrillo & Del Zanna 2004). A simple and cost-effective fifth-order scheme was proposed by adopting the hyperbolic divergence cleaning method (Dedner et al. 2002) by Mignone, Tzeferacos, and Bodo (2010). We have adopted a similar strategy, as described in the present paper.

The Coordinated Astronomical Numerical Software, CANS, was developed for the Japanese astrophysical community by T. Yokoyama at the University of Tokyo and collaborators, and is publicly available with documentation.¹ The base schemes are the modified Lax–Wendroff scheme and the CIP–MOCCT scheme (Kudoh et al. 1999; Yabe et al. 2001), but the Roe–MUSCL scheme is also available. Additional physics modules of heat conduction and radiative cooling, and many application modules, are also included. A physical problem can be easily solved by choosing the numerical schemes and visualizing by prebuilt Interactive Data Language (IDL) procedures, from which researchers and graduate students benefit when starting their simulation studies. CANS has been used in space and astrophysical applications since its introduction in 2002 (e.g., Asai et al. 2004; Isobe et al. 2005; Hanayama et al. 2005; Tao et al. 2005; Tsubouchi 2009; Toriumi & Yokoyama 2011).

CANS+ (CANS-plus) was designed based on the CANS philosophy, but has implemented current state-of-the-art numerical algorithms and parallelization. The code is written in Fortran90/95 and is organized in a modular way as in CANS. Hybrid parallelization is implemented

by using the Message-Passing Interface (MPI) library and OpenMP for effective parallel scaling on modern massively parallel supercomputer systems. Scripts for reading output data have been prepared for both Python and IDL languages so users can choose either of these environments for analysis. Sample programs for visualization in Python using the Matplotlib modules and IDL are also available for quick analyses. The code can be downloaded from the CANS+ documentation website.²

In this paper we detail the numerical algorithms adopted in CANS+ in section 2, and show assessments of the code's capability with various physical problems in section 3. As an application of CANS+, in section 4 we present three-dimensional (3D) global simulations of a black hole accretion disk and discuss how the selection of the numerical schemes affects the angular momentum transport and the resulting mass accretion rate during its long-term evolution. A summary of the paper and future perspectives are given in section 5.

2 CANS+

2.1 Basic equations

CANS+ solves the MHD equations in a normalized, semi-conservative form as

$$\frac{\partial \rho}{\partial t} + \nabla \cdot (\rho \mathbf{v}) = 0, \quad (1)$$

$$\frac{\partial \rho \mathbf{v}}{\partial t} + \nabla \cdot (\rho \mathbf{v} \mathbf{v} + p_t \mathbf{I} - \mathbf{B} \mathbf{B}) = \rho \mathbf{g}, \quad (2)$$

$$\frac{\partial \mathbf{B}}{\partial t} + \nabla \cdot (\mathbf{v} \mathbf{B} - \mathbf{B} \mathbf{v} + \psi \mathbf{I}) = -\nabla \times (\eta \mathbf{j}), \quad (3)$$

$$\frac{\partial e}{\partial t} + \nabla \cdot [(e + p_t) \mathbf{v} - \mathbf{B}(\mathbf{v} \cdot \mathbf{B})] = -\nabla \cdot (\eta \mathbf{j} \times \mathbf{B}) + \rho \mathbf{v} \cdot \mathbf{g}, \quad (4)$$

$$\frac{\partial \psi}{\partial t} + c_b^2 \nabla \cdot \mathbf{B} = -\frac{c_b^2}{c_p^2} \psi, \quad (5)$$

where ρ , \mathbf{v} , \mathbf{g} , \mathbf{B} , and e are the mass density, the velocity, the gravitational acceleration, the magnetic field, and the total energy density, respectively, \mathbf{I} is a unit tensor

$$\mathbf{I} = \begin{pmatrix} 1 & 0 & 0 \\ 0 & 1 & 0 \\ 0 & 0 & 1 \end{pmatrix}, \quad (6)$$

η is the resistivity, $\mathbf{j} = \nabla \times \mathbf{B}$ is the current density, and p_t represents the total (thermal and magnetic) pressure defined as

$$p_t = p + \frac{B^2}{2}. \quad (7)$$

¹ (<http://www-space.eps.s.u-tokyo.ac.jp/~yokoyama/etc/cans/>).

² (<http://www.astro.phys.s.chiba-u.ac.jp/cans/doc/>).

The thermal pressure p is given by

$$p = (\gamma - 1) \left(e - \frac{1}{2} \rho v^2 - \frac{B^2}{2} \right), \quad (8)$$

where γ is the specific heat ratio.

Equation (5) for ψ with equation (3) is introduced so that the solenoidal property of the magnetic field,

$$\nabla \cdot \mathbf{B} = 0, \quad (9)$$

is maintained within minimal errors during time integration (see subsection 2.4). Equations (1)–(5) complete the set of MHD equations that is conventionally referred to as GLM (generalized Lagrange multiplier) MHD equations (Dedner et al. 2002).

The GLM–MHD equations then read

$$\frac{\partial \mathbf{U}}{\partial t} + \sum_{s=x,y,z} \frac{\partial \mathbf{F}_s}{\partial s} = \mathbf{S}, \quad (10)$$

where

$$\mathbf{U} = (\rho \quad \rho \mathbf{v} \quad \mathbf{B} \quad e \quad \psi)^T \quad (11)$$

is a state vector of the conservative variables,

$$\mathbf{F}_s = \begin{pmatrix} \rho v_s \\ \rho v_s v_x + p_T \delta_{sx} - B_s B_x \\ \rho v_s v_y + p_T \delta_{sy} - B_s B_y \\ \rho v_s v_z + p_T \delta_{sz} - B_s B_z \\ v_s B_x - B_s v_x + \psi \delta_{sx} \\ v_s B_y - B_s v_y + \psi \delta_{sy} \\ v_s B_z - B_s v_z + \psi \delta_{sz} \\ (e + p_T) v_s - B_s (\mathbf{v} \cdot \mathbf{B}) \\ c_b^2 B_s \end{pmatrix} \quad (12)$$

and

$$\delta_{ij} = \begin{cases} 1 & (i = j) \\ 0 & (i \neq j) \end{cases}, \quad (13)$$

are a flux vector and the Kronecker delta, respectively, and

$$\mathbf{S} = \begin{pmatrix} 0 & \rho \mathbf{g} & -\nabla \times (\eta \mathbf{j}) & -\nabla \cdot (\eta \mathbf{j} \times \mathbf{B}) \\ & & & + \rho \mathbf{v} \cdot \mathbf{g} - \frac{c_b^2}{c_p^2} \psi \end{pmatrix}^T \quad (14)$$

is a source vector. We also define a vector \mathbf{V} for the primitive variables:

$$\mathbf{V} = (\rho \quad \mathbf{v} \quad \mathbf{B} \quad p \quad \psi)^T. \quad (15)$$

Let us consider equation (10) with $\mathbf{S} = 0$ in one dimension (1D; $s = x$). It can be written in the form

$$\frac{\partial \mathbf{U}}{\partial t} + A \frac{\partial \mathbf{U}}{\partial x} = \frac{\partial \mathbf{V}}{\partial t} + A_p \frac{\partial \mathbf{V}}{\partial x} = 0, \quad (16)$$

where

$$A = \frac{\partial \mathbf{F}_x}{\partial \mathbf{U}} \quad (17)$$

and

$$A_p = \left(\frac{\partial \mathbf{U}}{\partial \mathbf{V}} \right)^{-1} A \frac{\partial \mathbf{U}}{\partial \mathbf{V}} \quad (18)$$

are the Jacobian matrices for the conservative and the primitive variables, respectively, and

$$\frac{\partial \mathbf{U}}{\partial \mathbf{V}} = \begin{pmatrix} 1 & 0 & 0 & 0 & 0 \\ \mathbf{v} & \rho & 0 & 0 & 0 \\ 0 & 0 & 1 & 0 & 0 \\ \frac{\mathbf{v} \cdot \mathbf{v}}{2} & \rho \mathbf{v} & \mathbf{B} & \frac{1}{\gamma-1} & 0 \\ 0 & 0 & 0 & 0 & 1 \end{pmatrix} \quad (19)$$

is the quasilinear conversion matrix, which relates $\delta \mathbf{V}$ to $\delta \mathbf{U}$. Multiplying equation (16) by the matrix consisting of the left eigenvectors (L_p with $L_p \mathbf{R}_p = I$) of the Jacobian matrix gives the equation for the characteristic variables \mathbf{W} as

$$L_p \frac{\partial \mathbf{V}}{\partial t} + L_p A_p \mathbf{R}_p L_p \frac{\partial \mathbf{V}}{\partial x} = \frac{\partial \mathbf{W}}{\partial t} + \Lambda \frac{\partial \mathbf{W}}{\partial x} = 0, \quad (20)$$

where $\delta \mathbf{W} = L_p \delta \mathbf{V}$, and $L_p A_p \mathbf{R}_p = \Lambda = \text{diag}(\lambda_1, \lambda_2, \dots, \lambda_9)$ is a diagonal matrix containing the eigenvalues. For the GLM–MHD equations, $\lambda_1 - \lambda_9$ are

$$\lambda_{1,9} = \mp c_b, \quad \lambda_{2,8} = v_x \mp c_f, \quad \lambda_{3,7} = v_x \mp c_a, \quad \lambda_{4,6} = v_x \mp c_s, \quad \lambda_5 = v_x, \quad (21)$$

where

$$c_{f,s} = \left[\frac{\gamma p + |\mathbf{B}|^2 \pm \sqrt{(\gamma p + |\mathbf{B}|^2)^2 - 4\gamma p B_x^2}}{2\rho} \right]^{1/2} \quad (22)$$

refer to the fast (positive) and slow (negative) magnetosonic speeds, respectively, and

$$c_a = \frac{|B_x|}{\sqrt{\rho}} \quad (23)$$

is the Alfvén speed. In addition to the fast ($\lambda_{2,8}$), the Alfvén ($\lambda_{3,7}$), the slow ($\lambda_{4,6}$), and the entropy (λ_5) waves of the ideal MHD system, the GLM–MHD system introduces two waves with the eigenvalues (phase speeds) of $\lambda_{1,9} = \mp c_b$,

which represent omnidirectional propagation of numerical errors of the divergence-free condition [equation (9)].

2.2 Numerical algorithms

Time evolution of equation (10) for the state vector at a cell $U_{i,j,k}$ is obtained by the finite volume method,

$$\frac{\partial \bar{U}_{(i,j,k)}}{\partial t} = - \sum_{s=i,j,k} \frac{F_{(s+1/2)}^* - F_{(s-1/2)}^*}{\Delta_s} + S_{(i,j,k)} \equiv L(\bar{U}), \quad (24)$$

where \bar{U} is the cell-averaged value of U , Δ_s with $s = i, j, k$ represents the cell width in each dimension, $F_{(s\pm 1/2)}^*$ denotes a numerical flux at the cell surfaces, and $L(\bar{U})$ defines a numerical operator of the finite volume method. Equation (24) is integrated with time by the third-order strong-stability-preserving (SSP) Runge–Kutta (RK) scheme (Suresh & Huynh 1997; Gottlieb & Shu 1998):

$$\mathbf{u}^{(0)} = \bar{U}^n, \quad (25)$$

$$\mathbf{u}^{(1)} = \mathbf{u}^{(0)} + \Delta t^n L(\mathbf{u}^{(0)}), \quad (26)$$

$$\mathbf{u}^{(2)} = \frac{3}{4} \mathbf{u}^{(0)} + \frac{1}{4} [\mathbf{u}^{(1)} + \Delta t^n L(\mathbf{u}^{(1)})], \quad (27)$$

$$\mathbf{u}^{(3)} = \frac{1}{3} \mathbf{u}^{(0)} + \frac{2}{3} [\mathbf{u}^{(2)} + \Delta t^n L(\mathbf{u}^{(2)})], \quad (28)$$

$$\bar{U}^{n+1} = \mathbf{u}^{(3)}, \quad (29)$$

where the superscript n stands for a number of time steps and Δt^n is a corresponding step size. Δt^n is determined from the Courant–Friedrichs–Lewy (CFL) condition

$$\Delta t = \sigma_c \min_{i,j,k} \left[\frac{\Delta_i}{\max(|\lambda_{i2}|, |\lambda_{i8}|)}, \frac{\Delta_j}{\max(|\lambda_{j2}|, |\lambda_{j8}|)}, \frac{\Delta_k}{\max(|\lambda_{k2}|, |\lambda_{k8}|)} \right], \quad (30)$$

where $\lambda_{s,2,8}$ ($s = i, j, k$) is the eigenvalue for the fast magnetosonic wave calculated for each dimension, and σ_c is the CFL number. For the resistive MHD case, i.e., $\eta \neq 0$, Δt from equation (30) is again compared with the one determined from the diffusion number σ_d ,

$$\Delta t = \min \left[\Delta t, \sigma_d \min_{i,j,k} \left(\frac{\Delta_i^2}{\eta_{(i,j,k)}}, \frac{\Delta_j^2}{\eta_{(i,j,k)}}, \frac{\Delta_k^2}{\eta_{(i,j,k)}} \right) \right]. \quad (31)$$

In the following numerical experiments, $\sigma_c = \sigma_d = 0.3$ were adopted unless otherwise stated.

The numerical operator $L(\bar{U})$ is evaluated by following procedures.

(1) Conversion from the cell-averaged primitive variables to the characteristic variables locally (Harten et al. 1987). This operation is done by multiplying the primitive variables at cells within a stencil centered at a cell

(i, j, k) by the left eigenvector calculated at the cell (i, j, k) . For example, in the x -direction,

$$\mathbf{W}_{(i+q,j,k)} = \mathbf{L}_{p(i,j,k)} \bar{\mathbf{V}}_{(i+q,j,k)}, \quad (32)$$

with q varying from $-r$ to $+r$ for the $(2r + 1)$ th-order scheme. Among various eigenvectors, CANS+ adopts the same eigenvectors as the Athena code (Stone et al. 2008). Although this conversion is computationally expensive, separating waves according to the characteristics is necessary for obtaining nonoscillatory profiles by higher-order reconstructions as in the following.

(2) Reconstruction of the characteristic variables \mathbf{W} within a cell. To obtain high-resolution, nonoscillatory profiles, the fifth-order-monotonicity-preserving (MP5) interpolation scheme (Suresh & Huynh 1997) is used (see subsection 2.3). In the MP5 scheme, a five-point stencil ($r = 2$) is required for the conversion and the reconstruction steps. The interpolated values at both cell surfaces are obtained together in each dimension. For example, for a cell at (i, j, k) in the x -direction, the left-hand, right-state vector ${}^R\mathbf{W}_{(i-1/2,j,k)}$ and the right-hand, left-state vector ${}^L\mathbf{W}_{(i+1/2,j,k)}$ can be obtained for each interpolation procedure.

(3) The interpolated values at cell surfaces are then converted to the primitive variables using the local right eigenvector as

$${}^R\mathbf{V}_{(i-1/2,j,k)} = \mathbf{R}_{px(i,j,k)} {}^R\mathbf{W}_{(i-1/2,j,k)}, \quad (33)$$

$${}^L\mathbf{V}_{(i+1/2,j,k)} = \mathbf{R}_{px(i,j,k)} {}^L\mathbf{W}_{(i+1/2,j,k)}, \quad (34)$$

$${}^R\mathbf{V}_{(i,j-1/2,k)} = \mathbf{R}_{py(i,j,k)} {}^R\mathbf{W}_{(i,j-1/2,k)}, \quad (35)$$

$${}^L\mathbf{V}_{(i,j+1/2,k)} = \mathbf{R}_{py(i,j,k)} {}^L\mathbf{W}_{(i,j+1/2,k)}, \quad (36)$$

$${}^R\mathbf{V}_{(i,j,k-1/2)} = \mathbf{R}_{pz(i,j,k)} {}^R\mathbf{W}_{(i,j,k-1/2)}, \quad (37)$$

$${}^L\mathbf{V}_{(i,j,k+1/2)} = \mathbf{R}_{pz(i,j,k)} {}^L\mathbf{W}_{(i,j,k+1/2)}, \quad (38)$$

where \mathbf{R}_{ps} with $s = x, y, z$ represents the right eigenvector in each direction.

(4) Evaluation of the numerical flux F^* in each dimension by a Godunov-type scheme. That is, the numerical flux at a cell surface $(i + 1/2, j, k)$, for example, can be obtained from

$$\begin{aligned} F_{i+1/2}^* &= F(\bar{U}_i^n) - \frac{1}{\Delta t^n} \int_{x_i}^{x_{i+1/2}} \\ &\times U_R \left(\frac{x - x_{i+1/2}}{\Delta t}; {}^L\mathbf{V}_{i+1/2}, {}^R\mathbf{V}_{i+1/2} \right) dx \\ &+ \frac{x_{i+1/2} - x_i}{\Delta t^n} \bar{U}_i^n, \end{aligned} \quad (39)$$

where $U_R \left(\frac{x-x_{i+1/2}}{\Delta t}; {}^L\bar{V}_{i+1/2}, {}^R\mathbf{V}_{i+1/2} \right)$ is a solution inside the Riemann fan during a time interval of Δt with the initial conditions of the left (${}^L\mathbf{V}_{i+1/2}$) and right (${}^R\mathbf{V}_{i+1/2}$) states. (Here we have omitted (j, k) in the notation for simplicity.) CANS+ employs the HLLD approximate Riemann solver of Miyoshi and Kusano (2005), which gives accurate and robust solutions to Riemann problems. Note, however, that the equations for the magnetic field component normal to the cell surface and for ψ are decoupled from the seven remaining equations. The numerical flux values for these variables are easily obtained separately (see subsection 2.4).

- (5) The source term is evaluated at each Runge–Kutta substage [equations (26)–(28)].
- (6) Conversion from the updated conservative variables to the primitive variables.
- (7) Return to step 1.

2.3 The MP5 scheme

The MP5 scheme in the reconstruction step is based on a fourth-degree polynomial for each dimension. The left state of a quantity f at a cell $i + 1/2$ is first evaluated by

$${}^L f_{i+1/2} = \frac{2\bar{f}_{i-2} - 13\bar{f}_{i-1} + 47\bar{f}_i + 27\bar{f}_{i+1} - 3\bar{f}_{i+2}}{60}, \quad (40)$$

where \bar{f} is a cell-averaged value of f . The right state at $i - 1/2$ is also obtained at the same time from its symmetry in each dimension:

$${}^R f_{i-1/2} = \frac{2\bar{f}_{i+2} - 13\bar{f}_{i+1} + 47\bar{f}_i + 27\bar{f}_{i-1} - 3\bar{f}_{i-2}}{60}. \quad (41)$$

The original value results in a fifth-order spatially accurate solution in smooth regions, but an oscillatory profile around discontinuities. The MP5 scheme seeks a profile that degrades to the first order only around discontinuities. For this purpose, the original value is then brought to an interval using the median function

$${}^L f_{i+1/2} = \text{median}({}^L f_{i+1/2}, f_{\min}, f_{\max}). \quad (42)$$

Here the median function returns an intermediate value among the three arguments, so that the cell surface value lies in an interval between f_{\min} and f_{\max} . The basic concept is therefore the same as in standard TVD schemes. The TVD schemes with a three-point stencil, however, cannot distinguish between a discontinuity and a smooth profile around the extremum (figure 1). The interpolated value around the extremum of a sinusoidal profile (figure 1a) is then bounded by the neighboring cell values, resulting in strong damping of the waveform (figure 1b). Because of this difficulty, the TVD schemes have been applied mainly

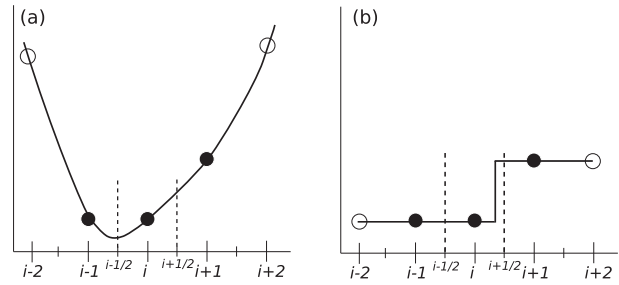


Fig. 1. Profile reconstructions around a cell i using different numbers of stencils (filled and open circles) for (a) parabola and (b) stair-step profiles. The vertical dashed lines indicate cell boundaries where reconstructed data are needed. This figure is adapted from figure 2.1 in Suresh and Huynh (1997). (Color online)

to problems where strong shock waves dominate. Accuracy and monotonicity preservation of profiles are accomplished in the MP5 scheme by using two additional values at cells (open circles in figure 1) to distinguish between the two. The curvature of a profile can be calculated by using the five-point stencil, and the interval is expanded in cases when the profile is identified as a parabola. Analytic consideration of the monotonicity preservation under the SSP–RK time integration for a linear advection equation leads to the CFL number restriction $\sigma_c < 0.2$ in the MP5 scheme. In practice, $\sigma_c = 0.3$, which was adopted in the following numerical tests, still gives nonoscillatory results. Readers may consult the original article by Suresh and Huynh (1997) for detailed derivations of f_{\min} and f_{\max} , and the CFL restriction. The implementation of the MP5 scheme in CANS+ for practical uses is given in appendix 1.

2.4 Hyperbolic divergence cleaning method

Upwind schemes including the finite volume method always suffer from numerical errors of the solenoidal property of the magnetic field. This occurs because the Lorentz force term in the momentum equation [equation (2)] involves an acceleration term along the magnetic field arising from numerical errors of $\nabla \cdot \mathbf{B}$; that is,

$$-\nabla \cdot \left(\frac{|\mathbf{B}|^2}{2} \mathbf{I} - \mathbf{B}\mathbf{B} \right) = (\nabla \times \mathbf{B}) \times \mathbf{B} + \mathbf{B}(\nabla \cdot \mathbf{B}), \quad (43)$$

which eventually leads to undesired results and thus inhibits following the long-term evolution of multidimensional problems. To overcome this inherent problem in multidimensional MHD simulations, several approaches have been developed (Tóth 2000; Miyoshi & Kusano 2011). Among them, modern MHD simulation packages have adopted strategies to satisfy discretized forms of the divergence-free condition within machine round-off errors based on a family of UCT algorithms (Londrillo & Del Zanna 2004; Gardiner & Stone 2005; Mignone et al. 2007; Lee & Deane

2009; Miyoshi & Kusano 2011; Minoshima et al. 2015, 2019; Lee et al. 2017). In contrast, CANS+ adopts the hyperbolic divergence cleaning method (Dedner et al. 2002; Mignone et al. 2010), which transports and damps numerical errors of the divergence-free condition, so that the growth of errors is managed to be within minimal levels. More specifically, multiplying equation (5) by $\partial/\partial t$ and equation (3) by $\nabla \cdot$, one finds that the scalar potential ψ and $\nabla \cdot \mathbf{B}$ obey the telegraph equations

$$\frac{\partial^2 \psi}{\partial t^2} + \frac{c_b^2}{c_p^2} \frac{\partial \psi}{\partial t} - c_b^2 \nabla^2 \psi = 0, \quad (44)$$

$$\frac{\partial^2 (\nabla \cdot \mathbf{B})}{\partial t^2} + \frac{c_b^2}{c_p^2} \frac{\partial (\nabla \cdot \mathbf{B})}{\partial t} - c_b^2 \nabla^2 (\nabla \cdot \mathbf{B}) = 0, \quad (45)$$

where c_b and c_p are constants characterizing the propagation speed and the damping rate, respectively.

Equation (5) has a semiconservative form and thus its numerical solution can benefit from the same high-order scheme applied to the original MHD equations. Let us consider the corresponding equations:

$$\frac{\partial}{\partial t} \begin{pmatrix} B_s \\ \psi \end{pmatrix} + \begin{pmatrix} 0 & 1 \\ c_b^2 & 0 \end{pmatrix} \begin{pmatrix} \nabla \cdot \mathbf{B} \\ \partial \psi / \partial s \end{pmatrix} = \begin{pmatrix} 0 \\ -\frac{c_b^2}{c_p^2} \psi \end{pmatrix}. \quad (46)$$

The system equations without the source term on the right-hand side in each dimension are decoupled from the MHD equations, and have eigenvalues of $\lambda_{1,9} = \mp c_b$ and right eigenvectors of $(1 \pm c_b)^T$. As c_b is a constant, they are linear equations. Thus, the numerical flux at a cell surface is given as

$$F_s^* = \begin{pmatrix} \psi^* \\ c_b^2 B_s^* \end{pmatrix} = \begin{bmatrix} \frac{1}{2}({}^R \psi + {}^L \psi) - \frac{c_b}{2}({}^R B_s - {}^L B_s) \\ \frac{c_b^2}{2}({}^R B_s + {}^L B_s) - \frac{c_b}{2}({}^R \psi - {}^L \psi) \end{bmatrix}, \quad (47)$$

where ${}^L \psi$, ${}^L B_s$, ${}^R \psi$, and ${}^R B_s$ denote the left (L) and the right (R) states at the cell surface for each quantity, respectively. These can be obtained in the same manner as in the reconstruction step. The obtained numerical flux is added to the numerical flux from the HLLD Riemann solver.

The contribution from the source term $(0 - \psi c_b^2 / c_p^2)^T$ is then added in an operator-split fashion as

$$\psi^{(m)} = C_1^{(m)} \psi^{(0)} + C_2^{(m)} [\psi^{(m-1)} + \Delta t^n L_{\text{FV}}(\psi^{(m-1)})] \times \exp\left(-\frac{c_b^2}{c_p^2} \Delta t^n\right), \quad (48)$$

where C_1 and C_2 are the weighting coefficients, L_{FV} represents the finite volume differentiation in equation (46), and the superscripts on ψ , C_1 , and C_2 denote the Runge–Kutta substage (m) in equations (25)–(28).

The constants c_b and c_p can be arbitrarily defined. As c_b represents the propagation speed of numerical errors, it is typically determined from the CFL condition as

$$c_b = \min_{i,j,k} (\Delta_i, \Delta_j, \Delta_k) \frac{\sigma_c}{\Delta t^n}. \quad (49)$$

Then, c_p is determined from the relation $c_p^2 / c_b = \text{const.}$ so as to equal the transport and decay time scales. Numerical experiments have shown that $c_p = \sqrt{0.18 c_b}$ results in the best performance regardless of grid resolution (Dedner et al. 2002) and was adopted in CANS+.

2.5 Source terms

The source terms on the right-hand side of equations (2)–(4) are evaluated at the cell center at each Runge–Kutta substage. $(\eta \mathbf{j})$ and $(\eta \mathbf{j} \times \mathbf{B})$ in the resistivity terms are first evaluated at the cell center by the second-order finite difference for the current density $\mathbf{j} = \nabla \times \mathbf{B}$, then they are added as a numerical flux at the cell surface by the arithmetic mean of the two neighboring cell-center values. Therefore, the resistivity terms degrade the overall spatial accuracy because of its second-order representation (more details are shown in appendix 3).

2.6 Some prescriptions for numerical stability

Higher-order, multidimensional codes usually suffer from vanishing and negative values of the scalar variables (ρ and p). CANS+ ensures numerical stability by examining the following prescriptions.

- In the reconstruction step, first-order interpolation is applied for the scalar variables and the normal component of the vector fields:
 - if one of the scalar variables recovered from the interpolated characteristic variables at a cell surface resulted in a negative value, or
 - if one of the scalar variables at a cell centered in the five-point stencil was two orders of magnitude smaller than the other cell values.
- In the conversion step, the thermal pressure given by equation (8) is evaluated every time in the Runge–Kutta substage. If the pressure becomes negative, it is overwritten by the value in the previous substage. The pressure is also evaluated in terms of the plasma beta ($\beta = 2p/B^2$) so as to bound the minimum β value. CANS+ allows $\beta \geq \beta_{\min} = 0.001$. The total energy density is then updated by the new pressure value. Thus, it is not strictly conserved in CANS+, while mass conservation is satisfied.

These operations can provide stable solutions in rarefied and low- β plasma regions as demonstrated in the two-dimensional (2D) simulations of the Parker instability described in sub-subsection 3.2.4.

2.7 CANS+ in cylindrical coordinates

CANS+ in cylindrical coordinates (R, ϕ, z) is based on the equations in a semi-conservative form:

$$\frac{\partial}{\partial t} \begin{pmatrix} \rho \\ e \\ \psi \end{pmatrix} + \left[\nabla_{\text{cyl}} \cdot \begin{pmatrix} RF_R^\rho & RF_R^e & RF_R^\psi \\ F_\phi^\rho & F_\phi^e & F_\phi^\psi \\ F_z^\rho & F_z^e & F_z^\psi \end{pmatrix} \right]^T = \mathbf{S}^{(\rho, e, \psi)}, \quad (50)$$

$$\frac{\partial}{\partial t} \begin{pmatrix} \rho v_R \\ \rho R v_\phi \\ \rho v_z \end{pmatrix} + \left[\nabla_{\text{cyl}} \cdot \begin{pmatrix} RF_{RR}^{\rho v} & R^2 F_{R\phi}^{\rho v} & RF_{Rz}^{\rho v} \\ F_{\phi R}^{\rho v} & F_{\phi\phi}^{\rho v} & F_{\phi z}^{\rho v} \\ F_{zR}^{\rho v} & F_{z\phi}^{\rho v} & F_{zz}^{\rho v} \end{pmatrix} \right]^T = \begin{pmatrix} \frac{F_{\phi\phi}^{\rho v}}{R} \\ 0 \\ 0 \end{pmatrix} + \mathbf{S}^{\rho v}, \quad (51)$$

$$\frac{\partial}{\partial t} \begin{pmatrix} B_R \\ B_\phi \\ B_z \end{pmatrix} + \begin{pmatrix} \frac{\partial F_{RR}^B}{\partial R} + \frac{\partial F_{\phi R}^B}{R\partial\phi} + \frac{\partial F_{zR}^B}{\partial z} \\ \frac{\partial F_{R\phi}^B}{\partial R} + \frac{\partial F_{\phi\phi}^B}{R\partial\phi} + \frac{\partial F_{z\phi}^B}{\partial z} \\ \frac{\partial (RF_{Rz}^B)}{R\partial R} + \frac{\partial F_{\phi z}^B}{R\partial\phi} + \frac{\partial F_{zz}^B}{\partial z} \end{pmatrix} = \mathbf{S}^B, \quad (52)$$

where

$$\nabla_{\text{cyl}} = \begin{pmatrix} \frac{\partial}{R\partial R} & \frac{\partial}{R\partial\phi} & \frac{\partial}{\partial z} \end{pmatrix}, \quad (53)$$

and \mathbf{F}^U and \mathbf{S}^U are the flux and the source term [equation (14)] corresponding to each conservative variable ($U = \rho, \rho \mathbf{v}, \mathbf{B}, e, \psi$).

The conservation equations are discretized, for example, in the form

$$\frac{\partial \rho_{(i,j)}}{\partial t} = - \frac{R_{i+1/2} F_{R(i+1/2,j,k)}^{*\rho} - R_{i-1/2} F_{R(i-1/2,j,k)}^{*\rho}}{R_i \Delta R_i} - \frac{F_{\phi(i,j+1/2,k)}^{*\rho} - F_{\phi(i,j-1/2,k)}^{*\rho}}{R_i \Delta \phi_j} - \frac{F_{z(i,j,k+1/2)}^{*\rho} - F_{z(i,j,k-1/2)}^{*\rho}}{\Delta z_k}. \quad (54)$$

The source term inherent in a curvilinear coordinate system [the first term on the right-hand side of equation (51)] is evaluated by taking the arithmetic mean of cell-surface values as $(F_{\phi\phi}^{\rho v}(i, j-1/2) + F_{\phi\phi}^{\rho v}(i, j+1/2))/2$. This source term also

degrades the overall spatial accuracy because of its second-order representation.

Special care is taken in the MP5 reconstruction step for the code in cylindrical coordinates. Mignone (2014) showed that incorporating the curvature of the cell into the piecewise polynomial reconstruction, namely, the volume-weighted reconstruction, greatly improved the solutions near the origin of the coordinate axis (along the z -axis in cylindrical coordinates). This technique has been implemented in the cylindrical version of the code (more details are shown in appendix 2).

The cylindrical version of the code has been used in global simulations of accretion disks, as shown in section 4.

3 Code assessments

In this section we present results from numerical tests to assess CANS+ by comparing with results from the second-order MUSCL scheme with the monotized central (MC) limiter and the second-order SSP–RK scheme (Gottlieb & Shu 1998). For specific heat ratio, gravity, and resistivity, $\gamma = 5/3$, $\mathbf{g} = 0$, and $\eta = 0$ were adopted in the following tests unless otherwise stated.

3.1 One-dimensional problems

3.1.1 Alfvén wave propagation

The spatial resolution of the MP5 scheme in CANS+ was verified by 1D tests of circularly polarized Alfvén wave propagations with various numbers of computational cells per wavelength. We initially set the magnetic and velocity profiles as

$$\begin{aligned} B_x &= B_0, \\ B_y &= 0.1 B_0 \cos(2\pi x), \\ B_z &= 0.1 B_0 \sin(2\pi x), \\ V_y &= -B_y, \\ V_z &= -B_z, \end{aligned} \quad (55)$$

where we have used units of the system size $L_x = 1$, the background Alfvén speed $V_{A0} = 1$, and the Alfvén transit time $T_0 = L_x/V_{A0}$. The CFL number $\sigma_c = 0.05$ was adopted in the following analyses on spatial resolutions to minimize errors from the time integration. Otherwise, the solution becomes the third order of the SSP–RK scheme under fixed CFL conditions.

Figure 2a shows spatial profiles of B_z obtained by the MP5 (red) and the MUSCL scheme (blue). The wavelength is resolved with 16 cells. After five Alfvén transit times ($t = 5$), while the amplitude of the wave has decreased

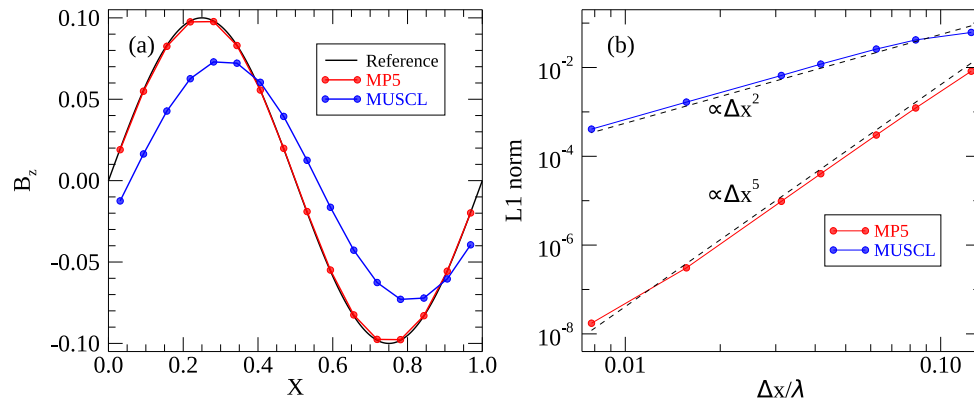


Fig. 2. Circularly polarized linear Alfvén wave propagation tests from MP5 (red) and MUSCL (blue) schemes. (a) B_z profiles after five Alfvén transit times ($t = 5$). The black curve indicates the analytic position of the wave. (b) L_1 norm errors obtained from numerical experiments with different grid resolutions. Dashed lines indicate the order of accuracy in space. (Color online)

by 25% in the MUSCL scheme, the profile from the MP5 scheme almost overlapped the theoretical profile (black). This strong damping of the wave is an inherent property of TVD schemes. In contrast, the MP5 scheme can detect smooth profiles and thus give a high-resolution result without modifying the original profile.

Numerical experiments with various cell widths gave the orders of accuracy of the schemes. Figure 2b shows the L_1 norms of the numerical errors from the MP5 (red) and the MUSCL (blue) schemes. The numerical errors increased with cell width according to the degree of the interpolation polynomial of each scheme. As expected, the dashed lines indicate that the MUSCL and the MP5 schemes have second- ($\propto \Delta x^2$) and fifth-order ($\propto \Delta x^5$) accuracy in space, respectively.

3.1.2 Shock tube problem

The monotonicity preservation of CANS+ was verified by a standard shock tube problem (Brio & Wu 1988; Ryu & Jones 1995). We initially set the values $(\rho, p, V_x, V_y, V_z, B_x, B_y, B_z)_L = (1, 1, 0, 0, 0, 0.75, 1, 0)$ in a region on the left-hand side of the simulation domain, $0 \leq x < 0.5$, and $(\rho, p, V_x, V_y, V_z, B_x, B_y, B_z)_R = (0.125, 0.1, 0, 0, 0, 0.75, -1, 0)$ on the right-hand side in $0.5 \leq x \leq 1$ with $\gamma = 5/3$ (Ryu & Jones 1995). We used 512 computational cells for this problem.

Figures 3a and 3d respectively show the ρ and V_x profiles at $t = 0.1$ obtained by CANS+ (red), and we compared them with the MUSCL scheme (blue) and the reference result obtained by the first-order scheme with 8192 cells (black). Characteristic profiles (from left to right: fast rarefaction, slow compound, contact discontinuity, slow shock, and fast rarefaction) were reproduced by CANS+. In particular, the contact discontinuity ($x \sim 0.56$) and the slow shock wave ($x \sim 0.63$) were resolved more sharply (figures 3b and 3e) than in the MUSCL scheme. A staircasing profile around

the compound wave can be found when the MP5 scheme was combined with the HLLD Riemann solver. A smoother profile was obtained with the HLL solver (not shown) as previously reported with the global Lax–Friedrichs scheme (Mignone et al. 2010).

Figures 3c and 3f compare the results from the MP5 scheme with different variables for the interpolation to cell surfaces. The reconstruction of the characteristic variables (black) that was used in CANS+ resulted in the best performance in capturing the discontinuities among the other variables used for the reconstruction, including the primitive variables shown in the figure (red). Interpolation of the characteristic variables, which were actually transported by the waves, was necessary for obtaining nonoscillatory results with the present fifth-order scheme.

3.2 Two-dimensional problems

3.2.1 Alfvén wave propagation

The capability of CANS+ was demonstrated with circularly polarized Alfvén wave propagation in two dimensions. By using various numbers of computational cells per wavelength, we verified the actual spatial resolution in multiple dimensions. We initially set the magnetic and velocity profiles as

$$\begin{aligned}
 B_l &= B_0, \\
 B_{t1} &= 0.1 B_0 \cos(2\pi l/\lambda), \\
 B_{t2} &= 0.1 B_0 \sin(2\pi l/\lambda), \\
 V_{t1} &= -B_{t1}, \\
 V_{t2} &= -B_{t2},
 \end{aligned} \tag{56}$$

where $\lambda = 1$ is the wavelength, l is the coordinate in the direction of the wave propagation, and $t1$ and $t2$ are

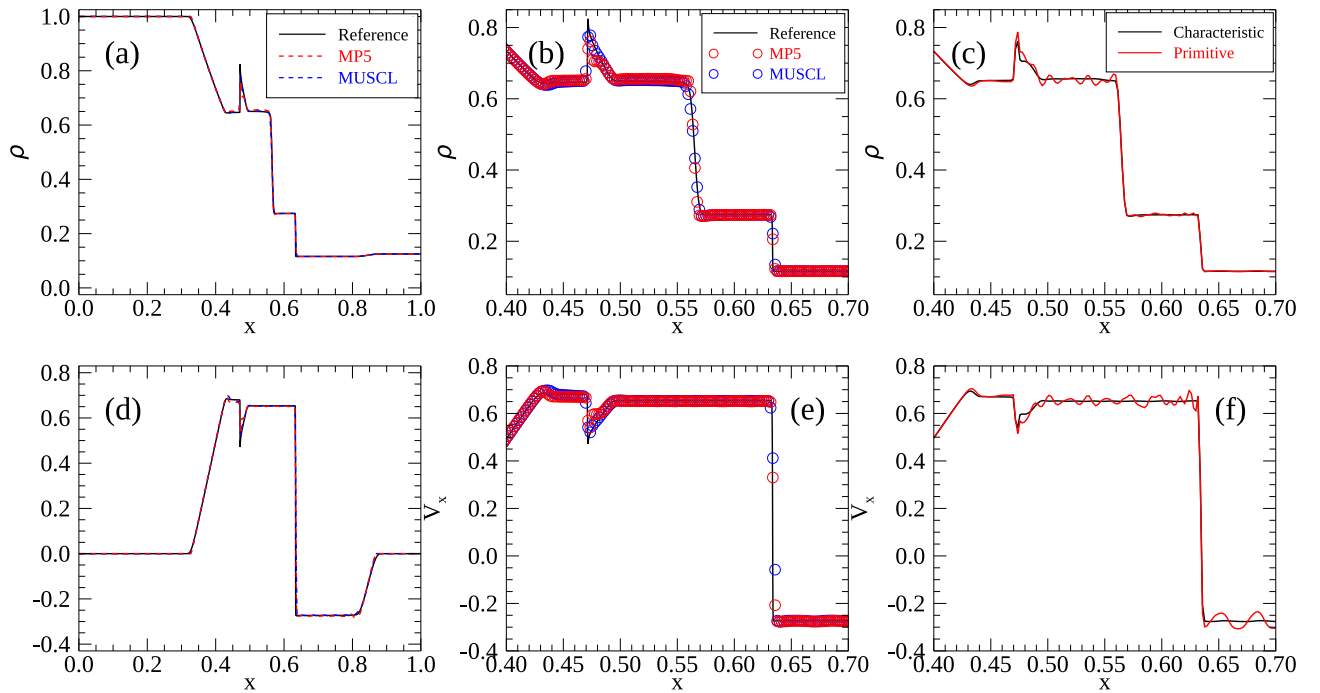


Fig. 3. Brio and Wu's shock tube problem: (a) and (b) show the mass density, and (d) and (e) the x -component of the velocity profiles for the MP5 (red) and MUSCL (blue) schemes. The reference result (black) was obtained by the first-order scheme using 8192 cells. Enlarged views of the mass density and velocity profiles are shown in (b) and (e), respectively. (c) and (f) compare the differences in mass density and velocity profiles arising from the MP5 reconstructions based on the characteristic (black) and primitive (red) variables. (Color online)

the transverse components. The x -, y -, and z -components of the magnetic field (velocity) are thus initially given as

$$\begin{aligned}
 B_x &= B_l \cos(\theta) - B_{t1} \sin(\theta), \\
 B_y &= B_l \sin(\theta) + B_{t1} \cos(\theta), \\
 B_z &= B_{t2},
 \end{aligned} \tag{57}$$

where θ is the propagation angle with respect to the x -axis. The simulation box sizes are $L_x = 1/\cos(\theta)$ and $L_y = 1/\sin(\theta)$. The CFL number $\sigma_c = 0.01$ was adopted to minimize errors from time integrations in the following analyses on spatial resolutions. We calculated numerical errors from the analytical solution after five Alfvén transit times along the propagation axis. In the following, results only with $\theta = 30^\circ$ are shown; however, we have confirmed that the resolution properties are similar when obtained with different propagation angles (see also appendix 1).

Figures 4a and 4b show spatial profiles of B_z obtained by the MP5 and MUSCL schemes, respectively. The wavelength is resolved with 16 cells in each direction. After five Alfvén transit times ($t = 5$), while the wave amplitude significantly reduced because the MC limiter is used in the MUSCL scheme, the initial wave amplitude was approximately retained when using the MP5 scheme with this spatial resolution.

Numerical experiments with various cell widths in figure 4c again show the high capability of the MP5 scheme in two dimensions. The errors from the MP5 scheme decreased as the cell size got smaller, following a slope expected from the fifth-order interpolation. It is also worth mentioning that the numerical errors are much larger in the MUSCL scheme than in the MP5 scheme when compared at the same cell size (figure 4c). In other words, the MP5 scheme can provide numerical solutions at the same accuracy with much coarser cells than those required in the MUSCL scheme. This result has great benefits for saving numerical costs because they increase as $\Delta x^{-(n+1)}$ in n -dimensional simulations, while the number of numerical operations in the MP5 scheme increases by a factor of two from those in the MUSCL scheme (see subsection 3.3).

3.2.2 The Kelvin–Helmholtz instability

Evolutions of the Kelvin–Helmholtz (K–H) instability in inhomogeneous plasma are presented as a multidimensional problem. We initially set the velocity shear profile as $V_x = -0.5V_0 \tanh(y/\lambda)$, where V_0 was 1.6 times the Alfvén speed V_A , λ was the half thickness of the velocity shear layer, and the mass density profile was set as $\rho = 0.5\rho_0[(1 - \alpha)\tanh(y/\lambda) + 1 + \alpha]$ with $\alpha = 0.1$. The magnetic field had only an out-of-plane component $\mathbf{B} = (0, 0, B_0)$. The system size in the x -direction (L_x) was equal to the wavelength of

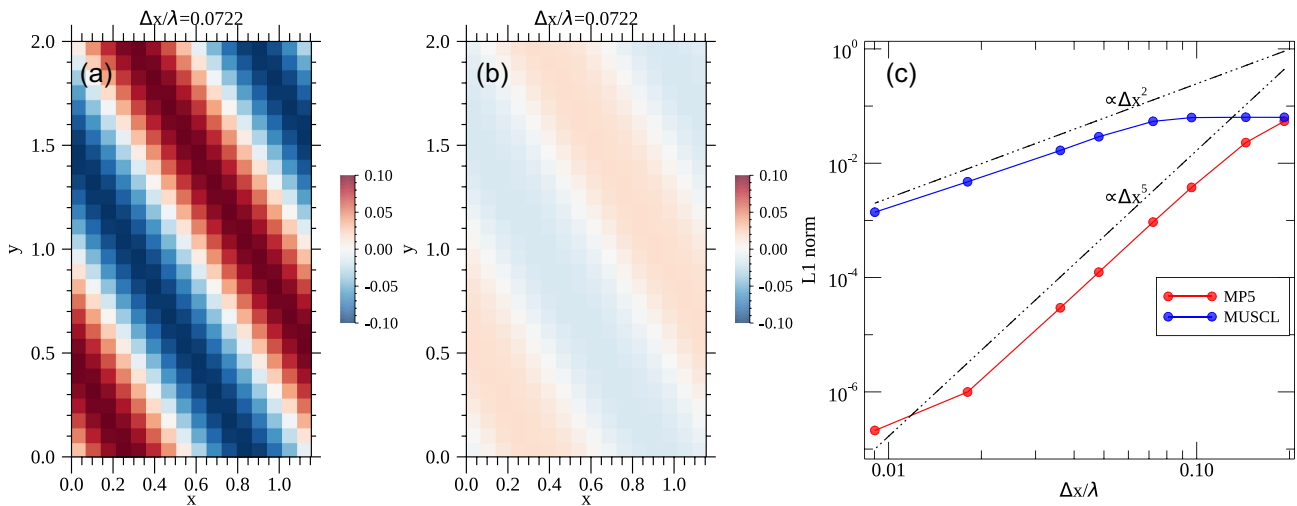


Fig. 4. Circularly polarized linear Alfvén wave propagation tests in the oblique propagation. B_z profiles after five Alfvén transit times are shown for (a) MP5 and (b) MUSCL schemes. The red–blue colorbar is scaled to the initial amplitude. (c) L_1 norm errors obtained from numerical experiments with different grid resolutions for the MP5 (red) and MUSCL (blue) schemes. The dashed lines indicate the order of accuracy in space. (Color online)

the fastest growing mode ($L_x = 11.2\lambda$) obtained by linear analysis for the present initial conditions (Matsumoto & Seki 2010). The system size in the y -direction (L_y) was in the range $-10\lambda \leq y \leq 10\lambda$ ($L_y = 20\lambda$). With these initial configurations, we added a sinusoidal perturbation to the y -component of the velocity inside the shear layer as $\delta V_y = 0.01 V_0 \sin(2\pi x/L_x) \cosh^{-2}(y/\lambda)$. Quantities were normalized to V_A , B_0 , ρ_0 , λ , and λ/V_0 . The computation domain was covered by 360×640 cells with λ being resolved by 32 cells. This initial configuration allowed us to benchmark the code’s capability to capture hydrodynamical turbulence along with the contact discontinuity.

Figure 5 shows the mass density profiles taken during nonlinear evolution with the MP5 (figures 5a and 5d) and MUSCL (figure 5e) schemes. Saturated K–H billows naturally formed sharp contact discontinuities, which eventually broke into turbulence via the secondary K–H and Rayleigh–Taylor instabilities (Matsumoto & Hoshino 2004). The fastest growing mode (FGM) grew exponentially at a rate of $\gamma_{\text{FGM}} = 0.09\lambda/V_0$ as expected from the linear analysis (figure 5b) in both results from the MP5 (solid) and MUSCL (dash–dot) schemes, whereas different behaviors in the nonlinear stage can be found for $t > 70$. A sharp mass density profile at $x = 8.4$ in the y -direction at $t = 55$ (figure 5c) verified that the MP5 scheme was capable of capturing the contact discontinuity and development of small-scale eddies at the same time precisely. Further development of the K–H turbulence contrasted the overall mixing efficiency between the different schemes. The MP5 scheme allowed the kinetic energy to be cascaded to small-scale vortices (figures 5d and 5f), whereas the MC limiter adopted in the MUSCL

scheme dissipated the cascaded energy at scales much larger than the cell size (figures 5e and 5f).

3.2.3 The Orszag–Tang vortex

We present results of the so-called Orszag–Tang vortex problem (Orszag & Tang 1979) to test the code’s capability of capturing shock–shock interactions and turbulence. We initiated the problem with $(\rho, p, V_x, V_y, V_z, B_x, B_y, B_z) = [\gamma^2, \gamma, -\sin(x), \sin(x), 0, -\sin(y), \sin(2x), 0]$ in the simulation domain of $0 \leq x, y \leq 2\pi$. The periodic boundary condition was applied in the x - and y -directions, and 200×200 cells were used to compare the results from the MP5 and MUSCL schemes. Results with 800×800 cells by the MUSCL scheme are also given as a reference run.

Figures 6a–6c show temperature ($T = P/\rho$) profiles from the MP5 (figure 6a) and MUSCL schemes (figure 6b). The overall structures seem to overlap with each other as characterized by sharp discontinuities at shock waves. Besides the overall structure, a closer look at the profile along the x -direction at $y = 0.5\pi$ (figure 6c) shows that the MP5 scheme (red filled circles) tended to follow the fine-scale structure of the reference run ($x \sim 0.75$, cyan line) but with an oscillatory profile, whereas a smooth profile was obtained by the MUSCL scheme (blue circles).

Figures 6d and 6e show the profiles of the divergence errors of the magnetic field. Here we introduced a normalized quantity defined by

$$\frac{|B \nabla \cdot B|}{\sqrt{(\nabla \cdot F^{*\rho v_x})^2 + (\nabla \cdot F^{*\rho v_y})^2}}, \quad (58)$$

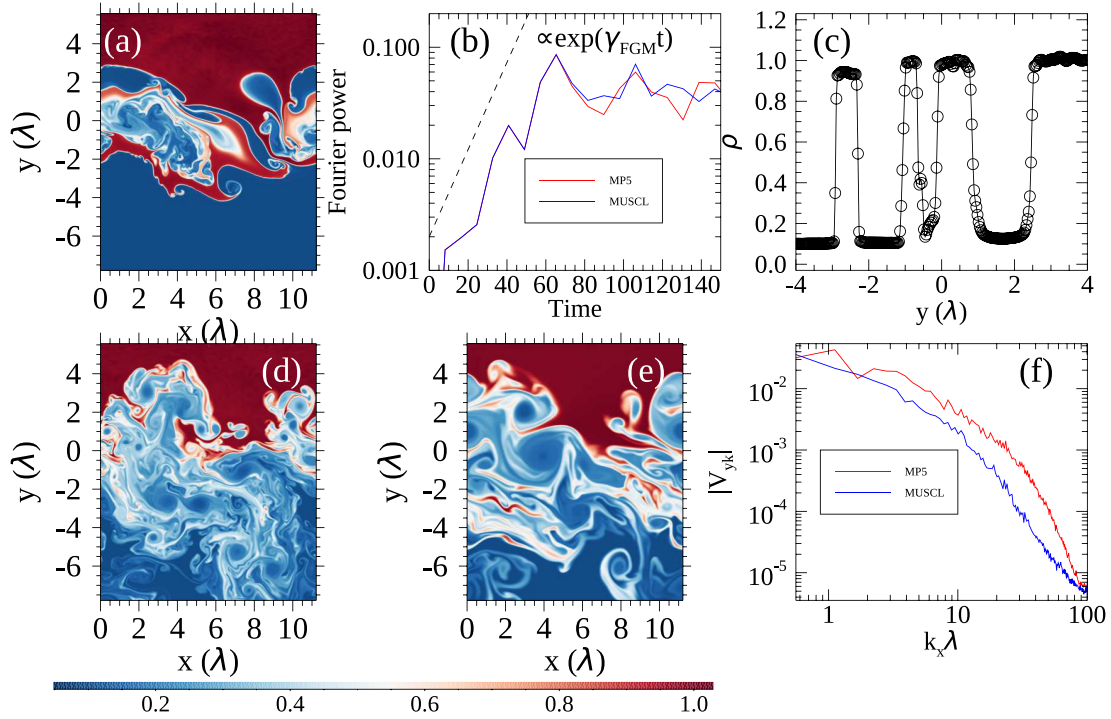


Fig. 5. Evolutions of the Kelvin–Helmholtz instability. (a) Mass density profile in the late linear growth phase at $t = 55$. (b) Time evolutions of the Fourier amplitude of the fastest growing mode of V_y from the MP5 (solid line) and MUSCL (dash–dot line) schemes. The dashed line indicates the linear growth rate obtained by Matsumoto and Seki (2010). (c) Mass density profile from the MP5 run in the y -direction at $x = 8.4$, $t = 55$. Mass density profiles from the (d) MP5 and (e) MUSCL schemes after the transition to turbulence at $t = 95$. (f) Spectra of the y -component of the velocity as a function of the wavenumber in the x -direction averaged over the simulation domain at $t = 95$ for the MP5 (solid line) and MUSCL (dash–dot line) schemes. (Color online)

where $F^{*\rho v_x}$ and $F^{*\rho v_y}$ denote the numerical flux for the x - and y -components of the momentum equations, respectively, to quantify the impact of the divergence errors on the dynamics [equation (43)]. Because CANS+ adopts the hyperbolic divergence cleaning method, non-negligible errors (a few to 10%) persist locally, in particular at shock wave fronts in both schemes. The errors are occasionally comparable to or greater than the physical force in very localized regions. This caveat that the divergence errors tended to be larger at shocks must be considered in multi-dimensional problems.

3.2.4 Parker instability

Magnetized plasma stratified under gravity becomes destabilized as a result of the buoyancy force against the magnetic tension force. This is known as the Parker instability (Parker 1966), and its nonlinear evolution is characterized by bent magnetic field lines in rarefied plasma (Matsumoto et al. 1988). We chose this problem as a benchmark test for evaluating the code’s capability to solve low- β plasma in multiple dimensions. In the present test, the gravity acceleration term g on the right-hand side of equation (2) was retained.

The Parker instability was initialized with the gravity acceleration profile

$$g = \left[0, -g_0 \tanh\left(\frac{y}{H_g}\right) \right] \quad (59)$$

and the temperature

$$T = T_0 + \frac{1}{2}(T_1 - T_0) \left[\tanh\left(\frac{|y| - y_0}{H_t}\right) + 1 \right]. \quad (60)$$

The mass density was determined from the static equilibrium

$$\frac{d}{dy} \left[(1 + \beta_0^{-1}) p \right] = \rho g, \quad (61)$$

where β_0 is the ratio of the thermal pressure to the magnetic pressure, and $p = \rho T / \gamma$. The magnetic field had only the x -component (B_x), with strength given by the plasma beta β_0 . The spatial length, velocity, and time were normalized to the scale height H_0 , the sound speed C_{s0} at $y = 0$, and the transit time H_0 / C_{s0} , respectively. Other quantities such as g , ρ , p , T , and B_x were normalized to C_{s0}^2 / H_0 , ρ_0 , $\rho_0 C_{s0}^2$, $C_{s0}^2 / (\gamma / m)$, and $\sqrt{\rho_0 C_{s0}^2}$, respectively. We adopted $\gamma = 1.05$,

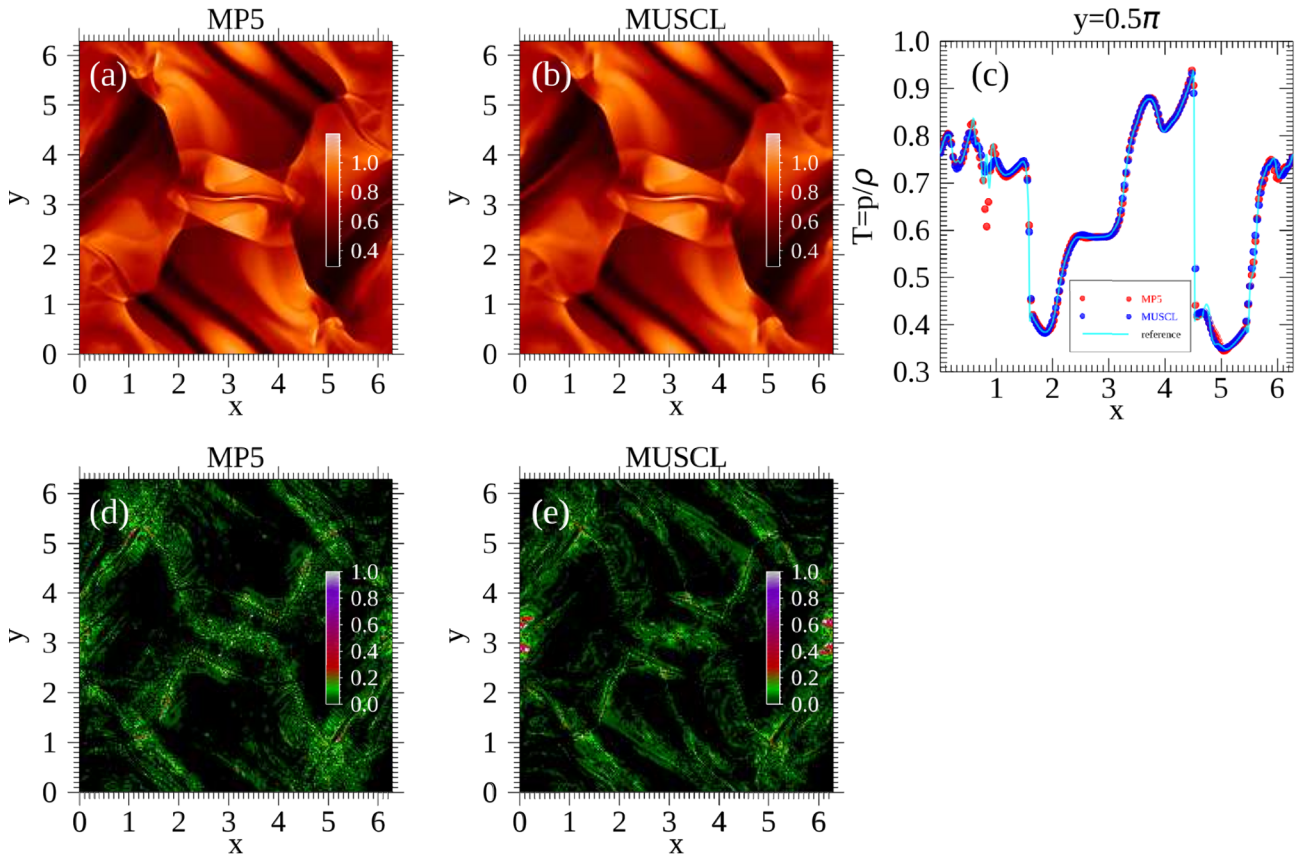


Fig. 6. Orsarg–Tang vortex problem. Temperature ($T = p/\rho$) profiles at $t = \pi$ are shown for the (a) MP5 and (b) MUSCL schemes. (c) Profiles in the x -direction at $y = 0.5\pi$ are compared between the MP5 (red filled circle) and MUSCL (blue open circle) schemes along with the result from the high-resolution run (800×800 cells) with the MUSCL scheme (cyan curve) as a reference. The normalized divergence errors of the magnetic field [equation (58)] are shown for the (d) MP5 and (e) MUSCL schemes, respectively. The color scale is saturated to 1.0 in panels (d) and (e). (Color online)

$g_0 = 1.47$, $H_g = 5.0$, $H_t = 0.5$, $y_0 = 10.0$, $T_0 = 1$, $T_1 = 25$, and $\beta_0 = 1.0$.

With these initial configurations, we added a perturbation to V_x in an antisymmetric form with respect to the $y = 0$ plane as

$$\begin{aligned} \delta V_x = & 0.05 \sin\left(\frac{2\pi x}{\lambda}\right) \\ & \times \left\{ \left[\tanh\left(\frac{y + y_2}{H_{pt}}\right) - \tanh\left(\frac{y + y_3}{H_{pt}}\right) \right] \right. \\ & \left. - \left[\tanh\left(\frac{y - y_2}{H_{pt}}\right) - \tanh\left(\frac{y - y_3}{H_{pt}}\right) \right] \right\}, \quad (62) \end{aligned}$$

where $y_2 = 4.0$ and $y_3 = 1.0$ restricted the perturbation in $1.0 \leq |y| \leq 4.0$, and $H_{pt} = 0.5$. $\lambda = 7.5\pi$ was chosen so that the wavelength of the applied perturbation corresponded to the FGM of the Parker instability under the present initial conditions (figure 7a). A benchmark test was conducted in a simulation domain of $-7.5\pi \leq x \leq 7.5\pi$ and $-15\pi \leq y \leq 15\pi$ with the periodic boundary condition in the x -direction

and the free boundary condition in the y -direction. The scale height H_0 was resolved by $20/\pi$ cells corresponding to the total number of cells of 300×600 .

Figure 7b shows the time evolution of the Fourier amplitude of the initial perturbation of the FGM. We found that the most unstable mode grew exponentially until $t = 50$ at the rate expected from the linear analysis (figure 7a).

In the nonlinear stage, magnetic loops were lifted up by the buoyancy force against the magnetic tension force. The plasma inside the loops fell down along the field lines creating high-density regions in the footpoints (figure 7c). The loop-top region therefore became rarefied in the nonlinear stage. The usual finite-volume methods based on the conservative form of the MHD equations eventually result in disastrous numerical solutions in such a rarefied, low- β plasma, but CANS+ successfully solved its evolution in which the mass density and the plasma β decreased down to $\sim 10^{-5}$ and $\sim 10^{-3}$ (figures 7c and 7d), respectively, in the late nonlinear stage by virtue of the prescriptions presented in subsection 2.6.

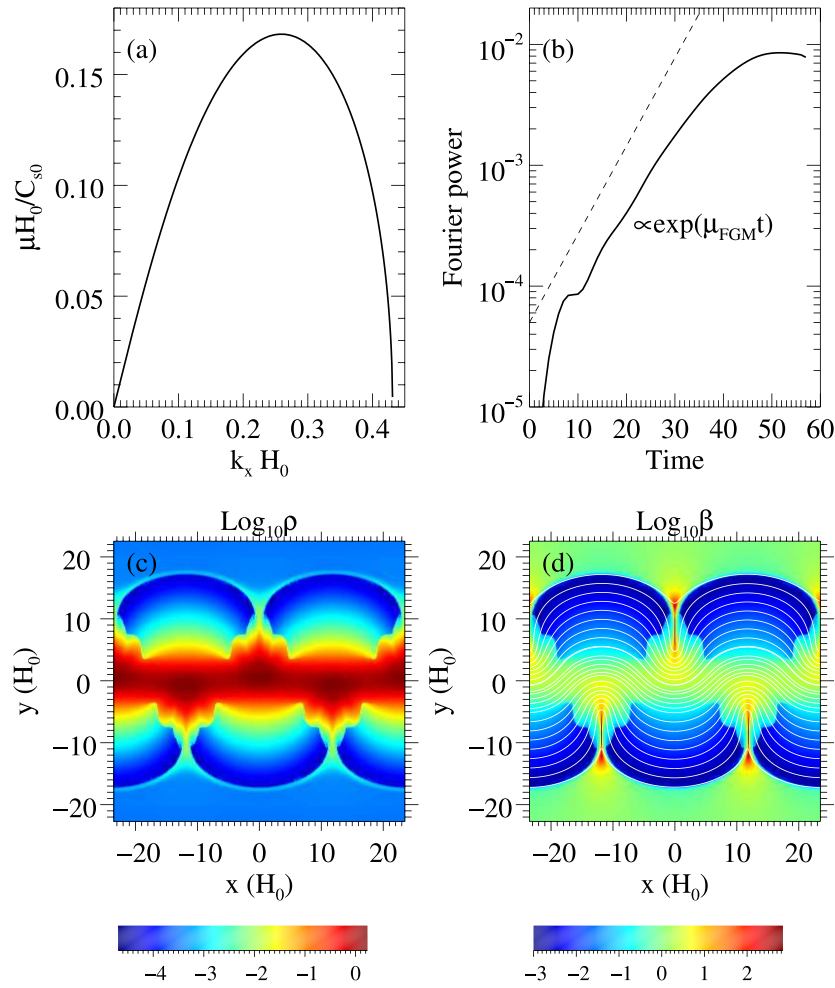


Fig. 7. (a) Linear growth rate of the Parker instability as a function of the wavenumber in the x -direction. (b) Time evolution of the Fourier power of the $m = 2$ mode (the FGM) of B_y by CANS+. The dashed line indicates the linear growth rate from the linear analysis in panel (a). (c) Mass density and (d) plasma β profiles at $T = 50$ in logarithmic scales. The magnetic field lines are represented by white solid lines in panel (d). (Color online)

3.2.5 Magnetic reconnection

When magnetic field lines are imposed to form an antiparallel geometry, the magnetic field topology changes through reconnection of the field lines. Because it accompanies magnetic energy conversion to the plasma kinetic energy, magnetic reconnection has been studied extensively to understand explosive phenomena, such as flares in the solar corona and pulsar winds, and terrestrial substorms. It is also an important part of the dynamo processes in accretion disks. The topology change during reconnection is characterized by bent magnetic field lines and bipolar trans-Alfvénic jets from the reconnecting “ x ” point, and the resulting plasmoid evolution. It was recently found by performing high-resolution MHD simulations that various MHD shock waves and discontinuities are formed as a result of interactions between the jet and plasmas surrounding the plasmoid (Zenitani & Miyoshi 2011; Zenitani 2015). Here we present the code’s capability to capture

such structures and turbulence associated with the plasmoid evolution. To initiate the reconnection, the resistivity η terms on the right-hand side of equations (3) and (4) were retained.

We examined simulation runs following Zenitani and Miyoshi (2011), in which the initial configurations were given as the Harris equilibrium: $B_x = B_0 \tanh(y/\lambda)$, $B_y = B_z = 0$, $\mathbf{V} = 0$, $\rho = \rho_0 [1 + \cosh^{-2}(y/\lambda)/\beta_0]$, and $p = 0.5 B_0^2 [\beta_0 + \cosh^{-2}(y/\lambda)]$, where λ is the current sheet half-thickness. The resistivity was locally added in the simulation domain around the “ x ” point as $\eta = \eta_0 + (\eta_1 - \eta_0) \cosh^{-2}(\sqrt{x^2 + y^2}/\lambda)$. Perturbations were initially added to the B_x and B_y components through the vector potential of $\delta A_z = 0.06 B_0 \lambda \exp[-(x^2 + y^2)/4\lambda^2]$. To save computation time, we only solved one quadrant of the reconnection region by applying symmetric conditions at $x = 0$ and $y = 0$. The simulation domain was therefore $0 \leq x \leq 200\lambda$ and $0 \leq y \leq 50\lambda$ with λ being resolved by 30 computational

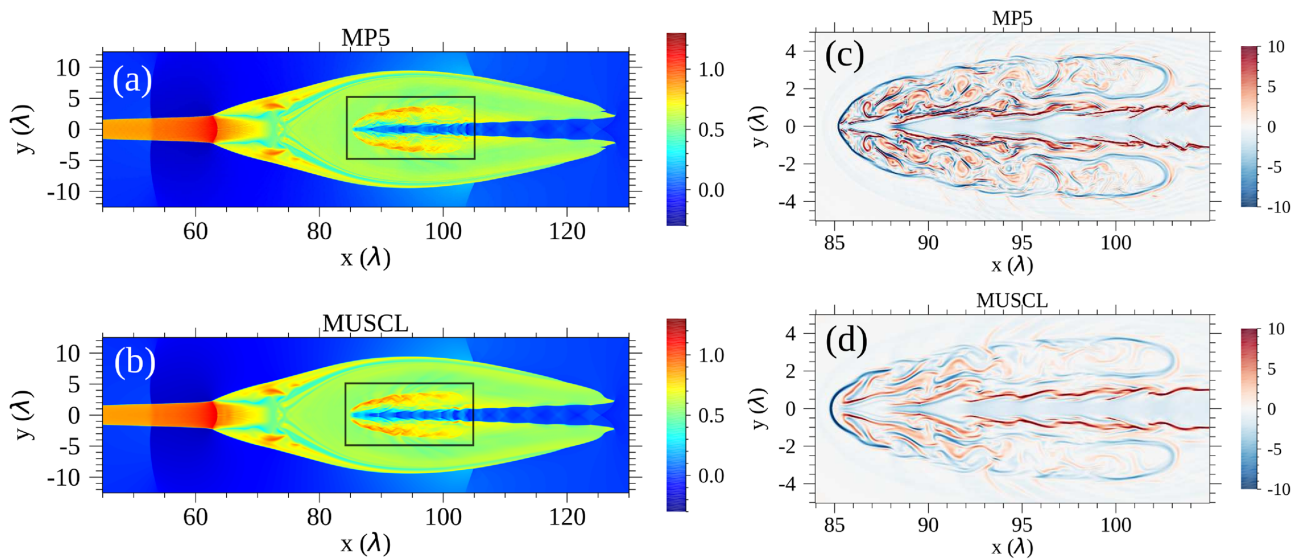


Fig. 8. (a) and (b) Profiles of the x -component of the velocity at $T=250$ for the MP5 and MUSCL schemes, respectively, characterizing the heart-shaped structure of the plasmoid downstream of the reconnection region. A mirrored image in $y < 0$ is also shown for visual purposes. (c) and (d) Enlarged views of the z -component of the current density ($\nabla \times \mathbf{B}$) in the open box area in panels (a) and (b) for the MP5 and MUSCL schemes, respectively. The color scale is saturated at ± 10 to visually identify fine-scale structures inside and around the jets. (Color online)

cells (6000×1500 cells). The spatial length, velocity, and time were normalized to λ , $V_{A0} = B_0/\sqrt{\rho_0}$, and λ/V_{A0} with $B_0 = \rho_0 = 1.0$, $\beta_0 = 0.2$, and $\eta_1 = 1/60$. We set $\eta_0 = 0.0$ to highlight the code's capability.

Figure 8 shows the V_x profiles at $t = 250$ characterizing a heart-shaped plasmoid structure downstream of the reconnection region. The plasmoid is formed as a result of interaction between the collimated jet from the reconnection region ($V_x > \sim 1$ at $x < 62$ and $-3 < y < 3$) and the stationary plasma in the current sheet. Vertical slow shock wave fronts in the outer ($x \sim 104$) and post-plasmoid ($x \sim 53$) regions, and multiple reflections of shock waves (shock diamonds) in the current sheet ($105 \leq x \leq 127$), were clearly captured by both the MP5 and MUSCL schemes (figures 8a and 8b) in addition to the various MHD discontinuities and shock waves, as reported previously (Zenitani & Miyoshi 2011).

The plasmoid motion in the x -direction pushes the stationary plasma away from the current sheet for $85 < x < 88$ to $y \sim \pm 2$, making the velocity shear between the swept and surrounding plasmas. This velocity profile can be a source of turbulence through excitation of the K–H instability (Zenitani & Miyoshi 2011). Figures 8c and 8d show enlarged views of the z -component of the current density ($\nabla \times \mathbf{B}$) in the area surrounded by dashed lines in figures 8a and 8b. In figure 8c, one can see a series of oblique red lines at $90 < x < 100$, $y = \pm 4$. They correspond to small shocks in front of the humps of the K–H waves. Although the large-scale pictures looked similar in the MP5 and MUSCL runs (figures 8c and 8d), the MP5 scheme resolved both the

shocklets and the highly turbulent current vortices much better.

3.3 Parallel scaling and computation efficiency

Hybrid parallelization is implemented in CANS+ using the MPI library and OpenMP. The code has been optimized to run effectively on massively parallel supercomputer systems. We examined the parallel efficiency of the 3D code on the K computer at the RIKEN Center for Computational Science, Reedbush at the Information Technology Center, the University of Tokyo, and ATERUI II at the Center for Computational Astrophysics, National Astronomical Observatory of Japan.

The K computer is composed of 82944 computation nodes, and each node has eight processor cores. A node's peak performance is 128 GFLOPS (128×10^9 floating-point operations per second). For this system, intra- and internode communications were respectively realized by OpenMP directives and MPI libraries.

The Reedbush and ATERUI II systems are based on many Intel Xeon CPUs. The Reedbush system is composed of 420 computation nodes, and each node has 36 processor cores (18 cores \times 2 CPUs). The ATERUI II system is composed of 1005 nodes, each of which has 40 cores (20 cores \times 2 CPUs). A node's peak performance is 1.2 TFLOPS (1.2×10^{12} FLOPS) and 3.1 TFLOPS, respectively. For the two systems, four MPI processes and eight OpenMP threads were used in each computation node.

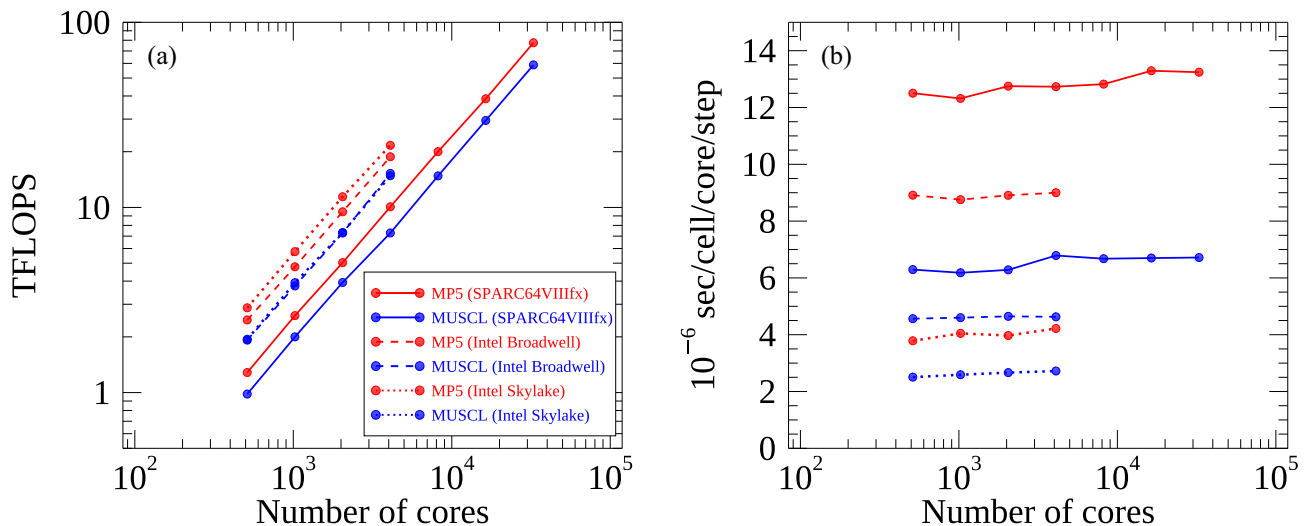


Fig. 9. (a) Parallel scaling of CANS+ code with different numbers of processor cores. (b) Computation speed of the code in terms of time taken for updating variables at a cell per core per time step. (Color online)

Figure 9 shows a benchmark result without data I/O functions after 5 min runs (approximately 3000 time steps with the MP5 scheme on the K computer). The scaling was obtained with a fixed number of cells of $64 \times 16 \times 64$ per MPI process (weak scaling) by using 512–32768 processor cores (64–4096 MPI processes) on the K computer, 512–4096 cores (64–512 MPI processes) on the Reedbush and the ATERUI II systems. The computation speed increased almost linearly with increasing numbers of cores up to 32768 on all systems, achieving a parallel efficiency of 94.4% for the MP5 scheme on the K computer (red solid line in figure 9a). The code with the MUSCL scheme also sped up linearly with increasing numbers of cores (93.6% efficiency, blue solid line).

With the help of the core’s SIMD (single instruction multiple data) capability, CANS+ also runs efficiently with respect to the system’s performance. The code with the MP5 scheme ran at 15.3% on average of the peak performance of the K computer with the tested numbers of cores, whereas the code with the MUSCL scheme ran at 11.6%; the MP5 reconstruction is an efficient scheme in terms of floating-point operations. The performance on other systems with smaller BF ratios (ratio of memory bandwidth to FLOPS) resulted in lower efficiencies of 13.9% (MP5) and 10.9% (MUSCL) on the Reedbush system, and 7.2% (MP5) and 4.8% (MUSCL) on the ATERUI II system.

Figure 9b shows the actual computation time during MHD simulations with various numbers of processor cores. Despite additional numerical costs including the three-stage SSP–RK time integration, the code with the MP5 scheme runs at $12.8 \mu\text{s core}^{-1}$ on average for updating the MHD variables in a cell in one time step on the K computer. This time is only twice as

large as with the MUSCL scheme with the two-stage SSP–RK integration ($6.5 \mu\text{s cell}^{-1} \text{ core}^{-1} \text{ step}^{-1}$), because of the high performance in the floating-point operations with the MP5 scheme. The code certainly runs faster on newer systems of the Reedbush (8.8 and $4.6 \mu\text{s cell}^{-1} \text{ core}^{-1} \text{ step}^{-1}$, respectively) and the ATERUI II (4.0 and $2.6 \mu\text{s cell}^{-1} \text{ core}^{-1} \text{ step}^{-1}$, respectively). Note, however, that the ratio of the computation time of the MP5 run to the MUSCL run decreased from $12.8/6.5 \sim 2.0$ on the K computer to $4.0/2.6 \sim 1.5$ on the latest low-BF-ratio system. The performance results and corresponding system specifications are summarized in table 1.

Because the MP5 reconstruction implemented in CANS+ requires more floating-point operations per cell than for the second-order MUSCL scheme, it is essentially less memory-intensive code. In other words, the code takes less time to load the required data from the physical memory than for the floating-point operations. This is a good property for recent low-BF-ratio systems. In general, the high-resolution (greater than the fifth order) code is suitable for massively parallel, petascale to exascale supercomputer systems because of its high efficiency.

4 Application to global simulations of a black hole accretion disk

In this section we present global simulations of an accretion disk around a black hole as an application of CANS+. The long-term evolution is characterized by a sharp contact discontinuity between the hot, dilute corona and the cold, dense, rotating disk, compressible magnetic turbulence via the magnetorotational instability (MRI), the resulting mass accretion (advection), and the periodic dynamo process

Table 1. Computation efficiency and system specifications.

	K computer	Reedbush	ATERUI II
CPU	Fujitsu SPARC64VIIIfx	Intel Xeon Broadwell-EP	Intel Xeon Skylake
BF ratio	0.50	0.13	0.08
SIMD vector length (bits)	128	256 (AVX2)	512 (AVX512)
Compiler & options	mpifrtpx -Kfast, openmp -x100	mpiifort -O3 -xCORE-AVX2 -qopenmp	ftn* -O3 -h omp
Computation efficiency [†] (MP5)	15.3%	13.9%	7.2%
Computation efficiency [†] (MUSCL)	11.6%	10.9%	4.8%
$\mu\text{s step}^{-1} \text{ core}^{-1} \text{ cell}^{-1}$ (MP5)	12.8	8.8	4.0
$\mu\text{s step}^{-1} \text{ core}^{-1} \text{ cell}^{-1}$ (MUSCL)	6.5	4.6	2.6

*The vendor-provided compiler (ftn) was used because it resulted in substantially better performances than the Intel compiler on this system.

[†]Percentage of peak performance.

through the Parker instability (Machida et al. 2013). All of these mechanisms were successfully solved by adopting the HLLD approximate Riemann solver, the MP5 reconstruction, and the hyperbolic divergence cleaning method in CANS+.

4.1 Initial torus model

We examined the evolution of an accretion disk in cylindrical coordinates (R, ϕ, z) initially given as a torus threaded by the toroidal magnetic field embedded in non-rotating, hot, and dilute plasma (corona) (Okada et al. 1989; Machida & Matsumoto 2003). General relativistic effects around the black hole are modeled by the pseudo-Newtonian gravitational potential (Paczynski & Wiita 1980),

$$\Phi = -\frac{GM}{r - r_s}, \quad (63)$$

where r is radial distance from the black hole in spherical coordinates, G is the gravitational constant, M is the black hole mass, and r_s is the Schwarzschild radius. Then the gravitational acceleration was obtained by $\mathbf{g} = -\nabla\Phi$.

The torus was initially given by setting a density profile (Nishikori et al. 2006) as

$$\rho_t = \rho_0 \left[\frac{\max(\Psi_0 - \Phi - L^2/2R^2, 0)}{K\gamma/(\gamma - 1) \left(1 + \beta_0^{-1} R^{2(\gamma-1)}/R_0^{2(\gamma-1)}\right)} \right]^{1/(\gamma-1)}, \quad (64)$$

where R_0 , ρ_0 , and β_0 are the values at the center of the torus at which the mass density has a maximum value, and $K = p_t/\rho_t^\gamma$ characterizes the polytropic relation between the gas pressure p_t and ρ_t inside the torus. L is the specific angular momentum in the functional form of

$$L = L_0 \left(\frac{R}{R_0}\right)^a, \quad (65)$$

where L_0 is the value of the Keplerian flow at R_0 and a is a constant. Ψ_0 is the potential energy at $R = R_0$ given by

$$\Psi_0 = \Phi_0 + \frac{L}{2R_0^2} + \frac{\gamma K}{\gamma - 1} \left(1 + \frac{1}{\beta_0}\right), \quad (66)$$

where Φ_0 is the gravitational potential at $r = R_0$. This potential energy is a constant provided the initial toroidal magnetic field is of the form (Okada et al. 1989)

$$B_\phi = \sqrt{\frac{2K}{\beta_0} \rho_t \left(\rho_t \frac{R^2}{R_0^2}\right)^{\gamma-1}}. \quad (67)$$

The mass density for the corona was given by (Nishikori et al. 2006)

$$\rho_c = \rho_{c0} \exp\left[-\frac{\gamma}{C_{sc}^2} (\Phi - \Phi_0)\right], \quad (68)$$

where $C_{sc} = \sqrt{\gamma p_c/\rho_c}$ is the characteristic sound speed in the corona. The total mass density is then given by $\rho = \rho_t + \rho_c$.

4.2 Numerical setup

The time evolution of the black hole accretion disk was obtained by the cylindrical version of CANS+ (see subsection 2.7). The spatial length, velocity, and time were normalized to the initial torus position (R_0), the rotating speed of the torus ($V_0 = L/R_0$), and the rotational period ($t_0 = 2\pi R_0/V_0$), respectively, and we will use units of $R_0 = V_0 = \rho_0 = 1$. In the following numerical experiments, we adopted $\gamma = 5/3$, $\beta_0 = 100$, $r_s = 0.1$, $K = 0.05$, $\rho_{c0} = 3 \times 10^{-4}$, and $C_{sc}^2 = 5.0$. L was set to be constant ($a = 0$) inside the torus. The number of computational cells in each direction was $(N_R, N_\phi, N_z) = (512, 128, 512)$. The cell sizes in the R - and z -directions were $\Delta R = 7.5 \times 10^{-3}$ for $0 \leq R \leq 3.0$ and $\Delta z = 7.5 \times 10^{-3}$ for $-1.5 \leq z \leq 1.5$. Outside these

regions, the cell sizes were increased by 5% with respect to the neighboring cell size as $\Delta R_{i+1}/\Delta R_i = \Delta z_{k+1}/\Delta z_k (z > 0) = \Delta z_{k-1}/\Delta z_k (z < 0) = 1.05$, where i and k are the cell number, and were bounded by a maximum value of 0.1. The cell size in the ϕ -direction was $\Delta\phi = 2\pi/N_\phi$. To save computation time, we set the innermost cell size to be $\Delta R_1 = 4\Delta R$. The computational domain consequently covered $0 \leq R \leq 9.4$, $0 \leq \phi \leq 2\pi$, and $-8.0 \leq z \leq 8.0$.

The periodic boundary condition was applied in the ϕ -direction, whereas the free boundary condition was applied in the z -direction and the outermost region in the R -direction. All physical quantities were absorbed inside the spherical region of $r \leq 0.2$. This was accomplished by damping the deviation of a physical quantity, q , from the initial state q_0 with a damping rate a_i as (Machida & Matsumoto 2003)

$$a_i = 0.1 \left[1.0 - \tanh \left(\frac{r - 0.2 + 5\Delta R}{2\Delta R} \right) \right], \quad (69)$$

$$q^{\text{new}} = q - a_i(q - q_0). \quad (70)$$

4.3 Results

4.3.1 MP5 vs. MUSCL schemes

Using the same initial setup, we compared the results for the MP5 and MUSCL schemes. Figure 10 shows the time evolution of the accretion disk solved by the MP5 scheme. Inside the torus threaded by the azimuthal magnetic field, the MRI grew exponentially (figures 10a, 10d, and 10g) until $t = 20$. The Maxwell stress ($B_R B_\phi$) generated by the MRI (figures 10d, 10e, 10g, and 10h) enhanced outward momentum transport, resulting in continuous mass accretion into the black hole (figures 10b and 10c).

After nonlinear saturation of the MRI, the poloidal component of the magnetic field was created via the Parker instability, allowing escape of magnetic flux to the corona, which in turn caused a reversal of the sign of the azimuthal component inside the disk (Machida et al. 2013). This reversal of the toroidal magnetic field occurred periodically during the long-term evolution in the simulation run with the MP5 scheme. Figure 11a shows a butterfly diagram for the azimuthal component of the magnetic field averaged in the region $0.2 \leq r \leq 0.5$ and $0 \leq \phi \leq 2\pi$. Reversals of the sign of the magnetic field at the disk center occurred after the preceding buoyant motions of the magnetic flux due to the Parker instability. This dynamo process persisted during the simulation run up to $t \sim 40$.

When we examined the same problem with the MUSCL scheme, such a dynamo process occurred in the late phase of the evolution, as shown in figure 11b. The TVD property of the MUSCL scheme evidently inhibited linear and

early nonlinear growth of the MRI. This drawback can also be seen in figure 12, in which the magnetic turbulence suffered from strong numerical damping in the early stage (figures 12a and 12d), and a global-scale magnetic field survived in the late nonlinear stage (figures 12c and 12f).

Figure 13a compares the time histories of the mass accretion rate calculated at the inner spherical boundary (cf. Stone & Pringle 2001)

$$\dot{M} = 2\pi r_0^2 \int_0^\pi \rho v_r \sin(\theta) d\theta, \quad (71)$$

where $r_0 = 0.2$ and θ are the radius at the inner boundary and the elevation angle in spherical coordinates, respectively. The mass accretion rate peaked at $t \sim 19$ and gradually decreased and maintained a certain level until $t = 50$ in the run with the MP5 scheme (red line). The mass accretion with the MUSCL scheme (blue line) followed a similar profile but peaked in the late stage of the simulation run because of slow growth of the MRI.

The mass accretion variations in time coincide with activities of the magnetic dynamo and turbulence in the disk, which can be quantified by the so-called α parameter (Shakura & Sunyaev 1973),

$$\alpha = -\frac{\langle B_R B_\phi \rangle}{\langle p \rangle}, \quad (72)$$

where $\langle \rangle$ stands for the volume-weighted average of the quantity in cylindrical coordinates. Figure 13b compares the time histories of the α parameter averaged in the region $0.2 \leq R \leq 0.5$, $0 \leq \phi \leq 2\pi$, and $-0.25\pi \leq \arcsin(z/\sqrt{r^2 + z^2}) \leq +0.25\pi$. As shown in the mass accretion variation, the α parameter was sustained at the level of $\alpha \sim 0.015$ following an initial peak of $\alpha \sim 0.1$ at $t = 19$ in the MP5 run (red line). The α parameter variation from the MUSCL run (blue line) exhibited a similar profile but with a peak in the late stage, as was found in the mass accretion rate variation.

4.3.2 Convergence test

We have examined the MP5 scheme under different spatial resolutions to assess the numerical convergence property for the present problem. The numerical parameters are summarized in table 2 for each spatial resolution.

Figure 14 shows the time evolution of the α parameter for runs with different resolutions in the same format as figure 13b. Whereas overall the profiles appear similar among runs with different resolutions, the initial growth of the MRI is slow in the low-resolution run (dotted line), as was found in the run with the MUSCL scheme (blue line

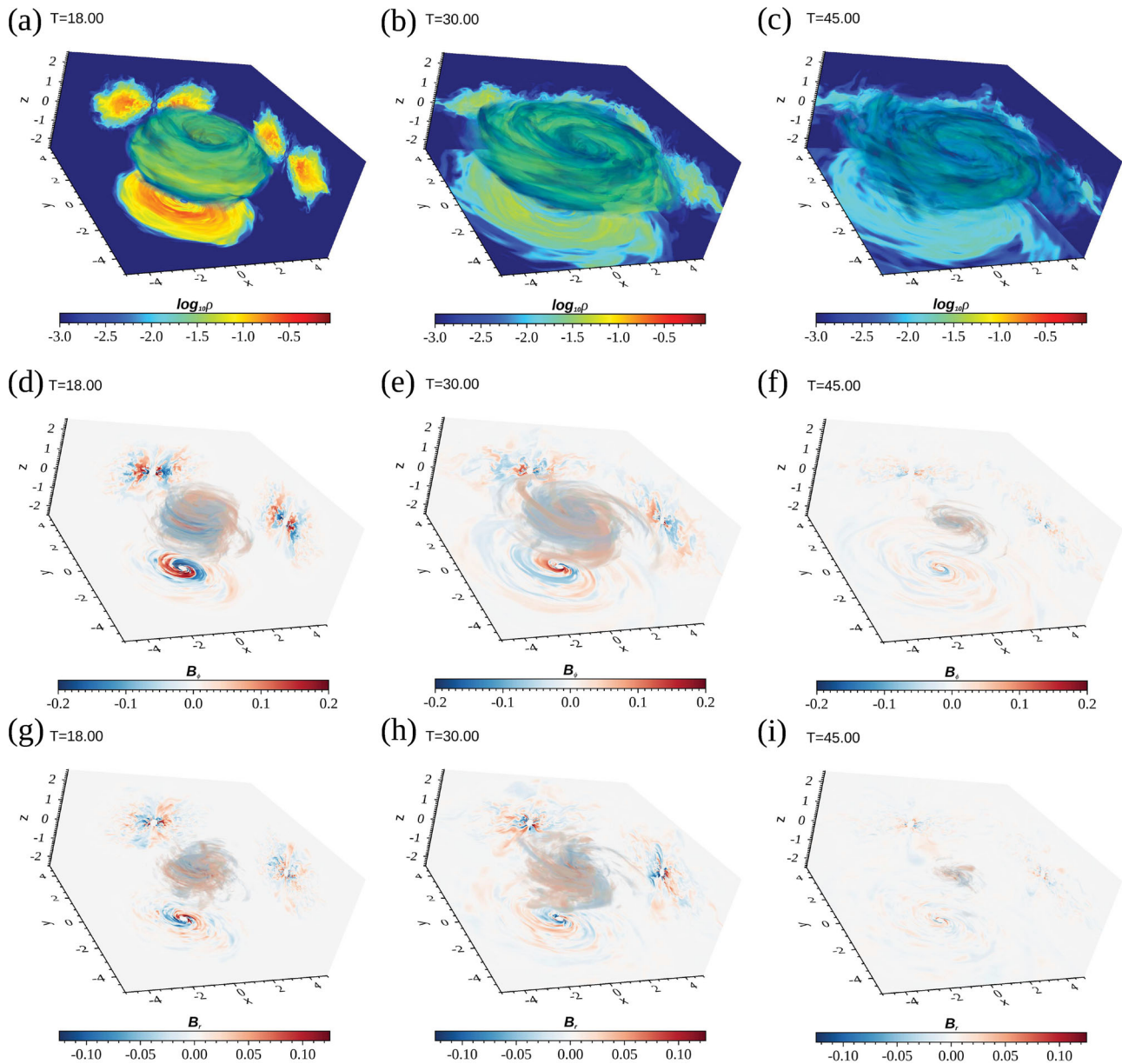


Fig. 10. Time evolution of the accretion disk obtained by the MP5 scheme. From left to right, snapshots at $t = 18.0$ (first column), $t = 30.0$ (second column), and $t = 45.0$ (last column) are shown for the mass density (top row) and ϕ - and R -components of the magnetic field (middle and bottom rows). The profiles at the equatorial and meridian planes passing through the black hole are projected on the x - y , x - z , and y - z planes. (Color online)

in figure 13b). We could obtain a convergent result of the MRI growth in the early stage up to $t \sim 10$ with medium (dashed line) and high (solid line) resolution runs. Nevertheless, the spatial resolution used in the high-resolution run is not high enough to give convergent results for further long-term evolution for $t > 10$.

5 Summary and discussion

We have developed CANS+, a high-resolution, numerically robust MHD simulation package, by employing

the HLLD approximate Riemann solver, the MP5 reconstruction method, and the hyperbolic divergence cleaning method. We performed a number of benchmark tests to show the code's capability for solving discontinuities, shock waves, and turbulence, all of which are particularly important in astrophysical situations.

In 1D benchmark tests that included linear Alfvén wave propagation and shock tube problems, the adoption of a spatial fifth-order scheme gave superior results compared with a second-order scheme, even when the additional computational costs arising from the higher-order

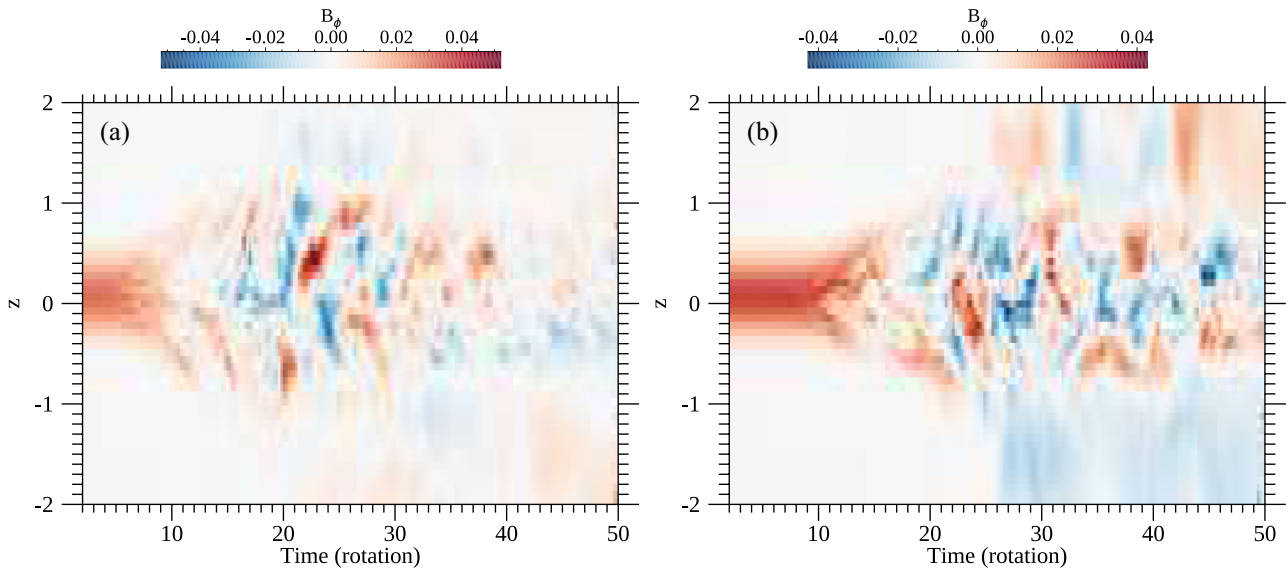


Fig. 11. Butterfly diagram for the azimuthal component of the magnetic field from the results of the (a) MP5 and (b) MUSCL schemes. (Color online)

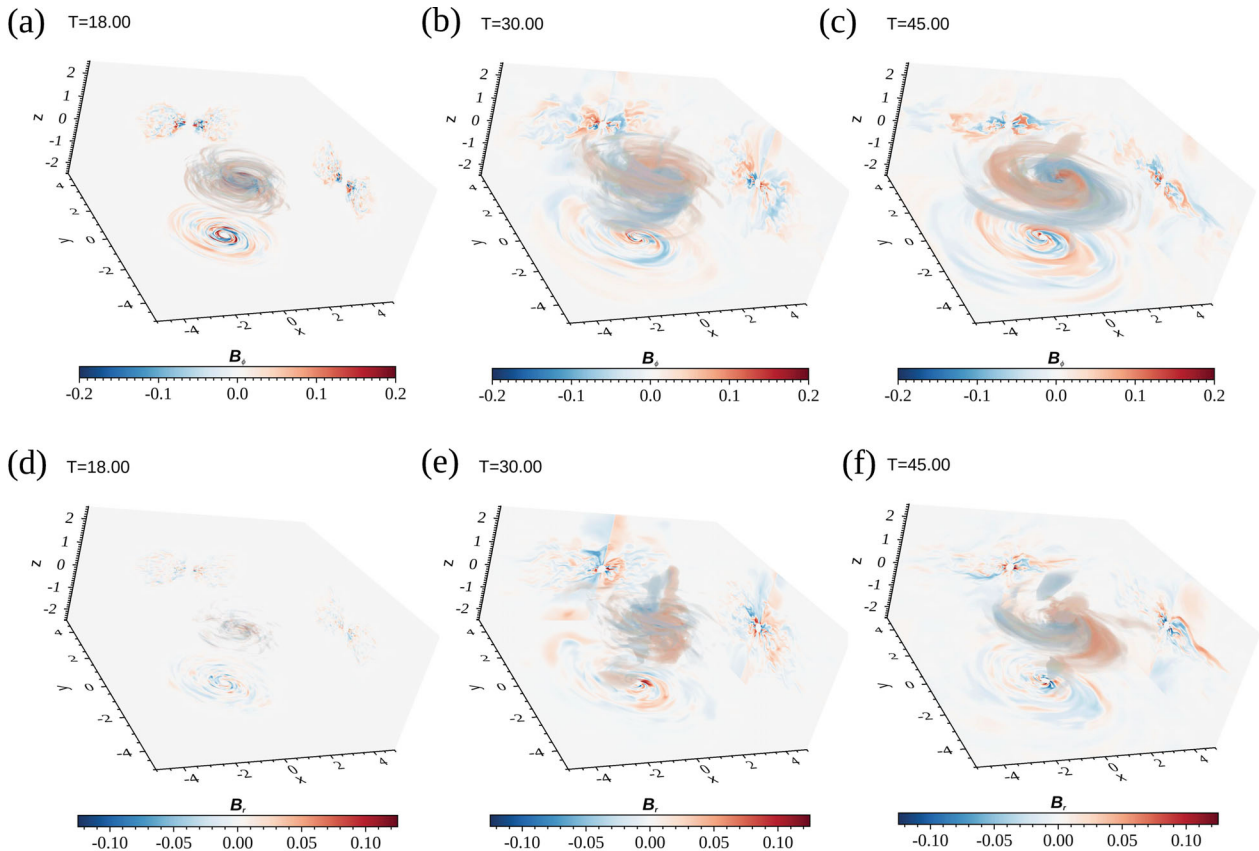


Fig. 12. Time evolution of the accretion disk obtained by the MUSCL scheme for the azimuthal [panels (a)–(c)] and the radial [panels (d)–(f)] components of the magnetic field. The format is the same as figures 10d–10i. (Color online)

reconstruction were considered: The computation time doubled compared with the second-order scheme, but for the same grid resolution the numerical errors from the fifth-order scheme were smaller by orders of magnitude. In other

words, to obtain solutions with the same accuracy, the fifth-order scheme required smaller numerical costs by orders of magnitude than the second-order scheme. This advantage is more prominent in multidimensional problems.

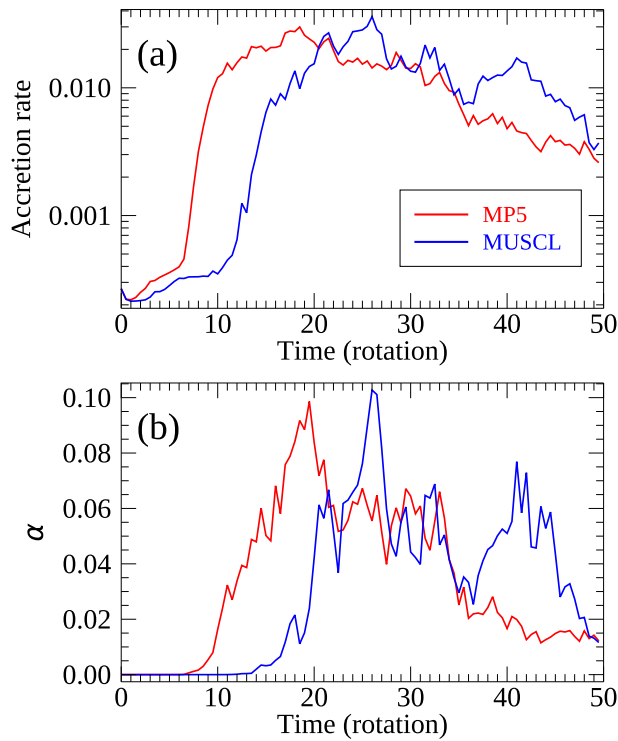


Fig. 13. Time evolution of (a) the absolute value of the mass accretion rate [equation (71)] and (b) the α parameter [equation (72)] obtained by the MP5 (red line) and MUSCL (blue line) schemes. (Color online)

In 2D tests of oblique Alfvén wave propagation, K–H turbulence, the Orszag–Tang vortex problem, and magnetic reconnection, it was shown that CANS+ enables solving discontinuities, shock waves, and turbulence with high accuracy and stability simultaneously. The test problem of the Parker instability also showed a high capability for solving very low- β ($\sim 10^{-3}$) plasma in which the numerical divergence errors of the magnetic field were maintained within reasonably low levels.

As an application of CANS+, we presented global simulations of an accretion disk around a black hole. With a given initial setup and grid resolution, CANS+ was capable of following the long-term evolution of the accretion disk in which the MRI and the resulting mass accretion into the black hole were sustained for 50 rotational periods. By increasing the spatial resolution, we could obtain a convergent result for the early nonlinear growth of the MRI.

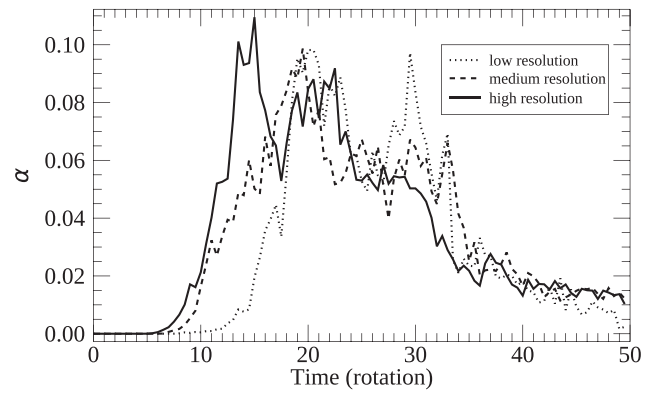


Fig. 14. Time evolution of the α parameter [equation (72)] obtained by the MP5 runs with different spatial resolutions. The dotted, dashed, and solid lines represent low-, medium-, and high-resolution runs, respectively. See also table 2.

The low-resolution run with the MP5 scheme gave a similar result to the medium-resolution run with the MUSCL scheme. Again, in practice, the MP5 scheme has at least twice the resolution of the MUSCL scheme, giving more than an eight times gain in computation time (more than 2^4 times speed-up with doubled computational costs) to obtain results with the same accuracy.

Lastly, we address the caveat of using fifth-order numerical schemes. The characteristic variables used for the reconstruction step showed the best performance with nonoscillatory results in the 1D shock tube problem. With other parameters, such as primitive variables, the updated conservative variable profiles were subject to numerical oscillations around discontinuities even if the MP5 reconstruction gave nonoscillatory profiles at cell surfaces. Thus, the reconstruction step not only required high computational costs because of the variable conversion, but also introduced difficulty in analytically obtaining the eigenvectors and the corresponding eigenvalues of the system. This can be problematic when extending the present MHD to, for example, the special relativistic MHD equations, in which second-order TVD schemes have been adopted (Matsumoto et al. 2011; Takahashi & Ohsuga 2013). The search for variables that are universally applicable to high-order reconstruction in various systems of equations remains a task for further applications of CANS+.

Table 2. Numerical parameters used for numerical convergence tests.

	Number of cells	ΔR	Δz	Range in R	Range in z
Low resolution	$256 \times 64 \times 256$	1.5×10^{-2}	1.5×10^{-2}	$0 \leq R \leq 7.5$	$-5.8 \leq z \leq 5.8$
Medium resolution*	$512 \times 128 \times 512$	7.5×10^{-3}	7.5×10^{-3}	$0 \leq R \leq 9.4$	$-8.0 \leq z \leq 8.0$
High resolution	$768 \times 192 \times 768$	5.0×10^{-3}	5.0×10^{-3}	$0 \leq R \leq 10.1$	$-8.8 \leq z \leq 8.8$

*Reference run.

Acknowledgments

CANS+ was based on the code originally developed by T. Ogawa at Chiba University. The numerical setup for magnetic reconnection was developed by N. Iwamoto, A. D. Kawamura, J. Sakamoto, and T. Shibayama during the simulation summer school held at Chiba University in 2014. The present simulations used computational resources provided by the Information Technology Center, the University of Tokyo, the Research Institute for Information Technology, Kyushu University, and the RIKEN Center for Computational Science through the HPCI System Research project (Project ID: hp120193, hp120287, hp130027, hp140213, hp140170, hp150263), and Cray XC50 at the Center for Computational Astrophysics, National Astronomical Observatory of Japan. This work was supported in part by MEXT SPIRE, MEXT as ‘‘Priority Issue on Post-K computer’’ (Elucidation of the Fundamental Laws and Evolution of the Universe), JICFuS, the Research Institute of Stellar Explosive Phenomena at Fukuoka University (JM), and JSPS KAKENHI Grant Numbers 16H03954 (RM) and 17K14260 (HRT).

Appendix 1. MP5 reconstruction in nonuniformly spaced cells

A piecewise fourth-degree polynomial is used in the MP5 reconstruction. For uniformly spaced cells, the left state of a quantity f at a cell $i + 1/2$ is, for example, given by

$$\begin{aligned} \bar{f}_{i+1/2} &= \frac{2\bar{f}_{i-2} - 13\bar{f}_{i-1} + 47\bar{f}_i + 27\bar{f}_{i+1} - 3\bar{f}_{i+2}}{60} \\ &= \sum_{r=0}^4 C_r \bar{f}_{(i-2+r)}, \end{aligned} \quad (\text{A1})$$

where

$$\bar{f}_i = \frac{1}{\Delta x_i} \int_{x_{i-1/2}}^{x_{i+1/2}} f(x) dx, \quad (\text{A2})$$

$$\Delta x_i = x_{i+1/2} - x_{i-1/2}. \quad (\text{A3})$$

For more practical uses, in which the cell size is not necessarily uniform, CANS+ employs the Lagrange polynomial

$$F(x) = \sum_{k=0}^5 \left(\prod_{l=0, l \neq k}^5 \frac{x - x_{i-5/2+l}}{x_{i-5/2+k} - x_{i-5/2+l}} \sum_{m=0}^{k-1} \bar{f}_{i-2+m} \Delta x_{i-2+m} \right) \quad (\text{A4})$$

to represent the spatial integral of the quantity f ,

$$F(x) = \int_{x_{i-5/2}}^x f(x') dx'. \quad (\text{A5})$$

Thus, f can be obtained by taking the derivative of equation (A4):

$$\begin{aligned} f(x) &= \frac{dF(x)}{dx} = \sum_{k=0}^5 \left[\prod_{l=0, l \neq k}^5 \frac{x - x_{i-5/2+l}}{x_{i-5/2+k} - x_{i-5/2+l}} \right. \\ &\quad \left. \times \sum_{m=0, m \neq k}^5 \frac{1}{x - x_{i-5/2+m}} \sum_{n=0}^{k-1} \bar{f}_{i-2+n} \Delta x_{i-2+n} \right]. \end{aligned} \quad (\text{A6})$$

Finally, the coefficients C_r in equation (A1) can be obtained for $x_{i+1/2}$ from $f(x_{i+1/2})$ as

$$\begin{aligned} C_r &= \sum_{k=1+r}^5 \left[\prod_{l=0, l \neq k}^5 \frac{x_{i+1/2} - x_{i-5/2+l}}{x_{i-5/2+k} - x_{i-5/2+l}} \right. \\ &\quad \left. \times \sum_{m=0, m \neq k}^5 \frac{1}{x_{i+1/2} - x_{i-5/2+m}} \Delta x_{i-3+k} \right]. \end{aligned} \quad (\text{A7})$$

Note that the C_r depend only on the cell size Δx_{i+n} and the cell surface’s location $x_{i+n/2}$. Thus, they can be determined at initialization.

A.1.1 Benchmark test

We examined circularly polarized Alfvén wave propagation in two dimensions using nonuniformly spaced cells as a benchmark test of the interpolation procedure of equation (A7). The initial setup is the same as that presented in sub-subsection 3.2.1, except that we adopted the propagation angle of $\theta = 45^\circ$. In this test, we used the following two different cell sizes:

$$\Delta x = \Delta y = \begin{cases} \Delta h_c & (0 \leq x, y \leq \frac{L_{x,y}}{3}, \frac{2}{3}L_{x,y} < x, y \leq L_{x,y}), \\ \frac{\Delta h_c}{2} & (\frac{L_{x,y}}{3} < x, y \leq \frac{2}{3}L_{x,y}), \end{cases} \quad (\text{A8})$$

where $L_{x,y}$ is the system’s size in the x - and y -directions.

By examining with different sizes of Δh_c , the accuracy of the code in nonuniformly spaced cells was obtained. We calculated the L_1 norm error by the following equation:

$$L_1 \text{ norm} = \frac{1}{L_x L_y} \sum_{i,j} \Delta x_{i,i} \Delta y_{j,j} |B_{z(i,j)} - B_{0(i,j)}|, \quad (\text{A9})$$

where (i, j) indicates the cell number in two dimensions and $B_{0(i,j)}$ is the analytic solution at each cell-center location.

Figure 15a shows the 2D profiles of the z -component of the magnetic field after five Alfvén transit times along with the cell shape. We determined that the code can solve smooth profiles in nonuniformly spaced cells without strong damping of the wave amplitude and large phase errors. Figure 15b shows the L_1 norm errors for various Δh_c for the nonuniform (orange line) cell cases. Here, we also plotted results from uniform cell cases (green line). We found that the error decreased following the slope expected from the fifth-order interpolation for $\Delta h_c/\lambda > 0.1$. We also note that the errors are smaller in the nonuniform cases than in the uniform cases. However, the accuracy curve approaches the slope of the second-order accuracy for $\Delta h_c/\lambda \leq 0.1$ in the nonuniform cases. The accuracy curve for the uniform cases followed the fifth-order slope all the way down to $\Delta h_c/\lambda \sim 0.01$, as expected from the results in sub-subsection 3.2.1.

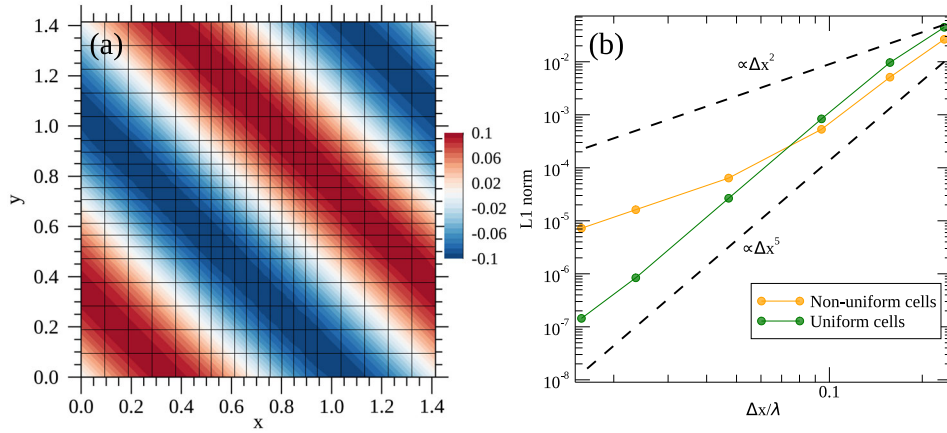


Fig. 15. Circularly polarized linear Alfvén wave propagation tests in the oblique (diagonal) propagation in nonuniformly spaced cells. (a) B_z profile after five Alfvén transit times along with the cell shape. (b) L_1 norm errors obtained from numerical experiments with different cell resolutions (Δh_c) for the uniform (green) and nonuniform (orange) cases. The dashed lines indicate the order of accuracy in space. (Color online)

Appendix 2. MP5 reconstruction in cylindrical coordinates

Mignone 2014 showed that incorporating the curvature of the cell into the piecewise polynomial reconstruction in curvilinear coordinates, namely, the volume-weighted reconstruction, improved the solutions near the origin of the coordinate axis (along the z -axis in cylindrical coordinates). This curvature effect is considered for the MP5 reconstruction in the R -direction in cylindrical coordinates. In this case, equations (A4) and (A5) are modified as

$$F(R) = \int_{R_{i-5/2}}^R R' f(R') dR' = \sum_{k=0}^5 \left(\prod_{l=0, l \neq k}^5 \frac{R - R_{i-5/2+l}}{R_{i-5/2+k} - R_{i-5/2+l}} \right) \times \sum_{m=0}^{k-1} \tilde{f}_{i-2+m} R_{i-2+m} \Delta R_{i-2+m}, \quad (\text{A10})$$

where

$$\tilde{f}_i = \frac{1}{R_i \Delta R_i} \int_{R_{i-1/2}}^{R_{i+1/2}} R f(R) dR, \quad (\text{A11})$$

$$R_i = \frac{R_{i+1/2} + R_{i-1/2}}{2}, \quad (\text{A12})$$

$$\Delta R_i = R_{i+1/2} - R_{i-1/2}. \quad (\text{A13})$$

As for Cartesian coordinates, the coefficients C_r are similarly obtained for $R_{i+1/2}$ from $f(R_{i+1/2}) = \frac{1}{R_{i+1/2}} \frac{dF}{dR} \Big|_{R=R_{i+1/2}}$ as

$$C_r = \frac{1}{R_{i+1/2}} \sum_{k=1+r}^5 \left[\prod_{l=0, l \neq k}^5 \frac{R_{i+1/2} - R_{i-5/2+l}}{R_{i-5/2+k} - R_{i-5/2+l}} \right] \times \sum_{m=0, m \neq k}^5 \frac{1}{R_{i+1/2} - R_{i-5/2+m}} R_{i-3+k} \Delta R_{i-3+k}. \quad (\text{A14})$$

Note that the coefficient for the right state of the cell surface at $R = 0$ becomes infinity. This singularity at $R = 0$ is

addressed by adopting the first-order reconstruction, i.e., ${}^R f_0 = \tilde{f}_1$.

A.2.1 Boundary condition at $R = 0$

In the following, we present results from benchmark tests to discuss how the two interpolation procedures of equations (A7) and (A14) result in different evolutions in cylindrical coordinates.

For boundary conditions across the z -axis, ρ , p , and (V_z, B_z) were assumed with axisymmetric profiles, whereas the antisymmetric boundary condition is applied to $(V_R, V_\phi, B_R, B_\phi)$ for the case with equation (A7) as usual. Conversely, with equation (A14), the symmetric and antisymmetric boundary conditions were applied to $(V_R, V_\phi, B_R, B_\phi)$ and (V_z, B_z) , respectively. We found that this somewhat odd boundary condition gave the best results with equation (A14) in the following experiments. The naive idea behind this is that a cell volume $R_i \Delta R_i$ becomes negative for $R < 0$ by definition [equations (A12) and (A13)], and the sign of the vector quantities should be reversed when constructing the volume-weighted polynomial. Note, however, that the usual boundary condition should be used for other situations, such as when calculating the current density (appendix 3). The special care for the boundary condition in cylindrical coordinates was also addressed in global simulations of a black hole accretion disk in section 4.

A.2.2 Benchmark tests

A.2.2.1 1D magnetic confinement of a cylindrical plasma column

First, we examined a static balance problem presented by Mignone (2014). In this test, a cylindrical plasma column was initially confined by the toroidal magnetic field of B_ϕ ,

satisfying a radial force balance between the gas pressure (p) gradient and the Lorentz forces, as shown in the following equations:

$$p = \frac{p_0}{(1 + R^2/R_0^2)^2}, \quad (\text{A15})$$

$$B_\phi = \frac{R\sqrt{2p_0}}{R_0(1 + R^2/R_0^2)}, \quad (\text{A16})$$

where $p_0 = 1$ at $R = 0$ and $B_\phi = 1/\sqrt{2}$ at $R_0 = 1$. The initial cell-averaged quantities were numerically obtained by Simpson's rule.

The solutions were obtained in a 1D domain in $0 \leq R \leq L_R$ for different spatial resolutions at a normalized time of $t = 10$. Here, the domain size was $L_R = 10$, and we used 32 to 1024 computational cells to obtain the spatial accuracy of the code. The CFL number was fixed at $\sigma_c = 0.05$.

For the present cylindrical case, the L_1 norm error was calculated by

$$L_1 \text{ norm} = \frac{1}{\Delta_{\text{cyl}}} \sum_i^{\max} R_i |V_{R,i}(t = 10) - V_{R,i}(t = 0)|, \quad (\text{A17})$$

where Δ_{cyl} is the cylindrical volume of a 1D domain $0 \leq R_i \leq R_{\text{max}}$:

$$\Delta_{\text{cyl}} = \int_0^{R_{\text{max}}} R dR = \frac{R_{\text{max}}^2}{2}, \quad (\text{A18})$$

and i indicates the cell number. To highlight the differences between the two schemes, we adopted $R_{\text{max}} = 1.0$. Obviously, $V_R(t = 0) = 0$ in the present static balance problem.

Figure 16 shows the L_1 norm errors with different spatial resolutions for the interpolations of equation (A7), the green line, and equation (A14), the orange line. The overall spatial accuracy follows the slope expected from the fifth-order interpolation, but the accuracy curve approaches the third order of the SSP-RK time integration in high-resolution runs ($0.004 < \Delta R/L_R$) under the fixed CFL condition. The error with the interpolation of equation (A7) is, however, about one order of magnitude larger than the error of the interpolation incorporating the cell's curvature effect [equation (A14)] in all spatial resolutions. We found great improvement in the solution, especially near the coordinate origin.

A.2.2.2 2D blast-wave propagation

Next we demonstrate a blast-wave propagation in a 2D (R - z) configuration. The initial setup is the same as that introduced by Mignone (2014), and constant background quantities were given as

$$\rho_0 = \frac{1}{4}, \quad (\text{A19})$$

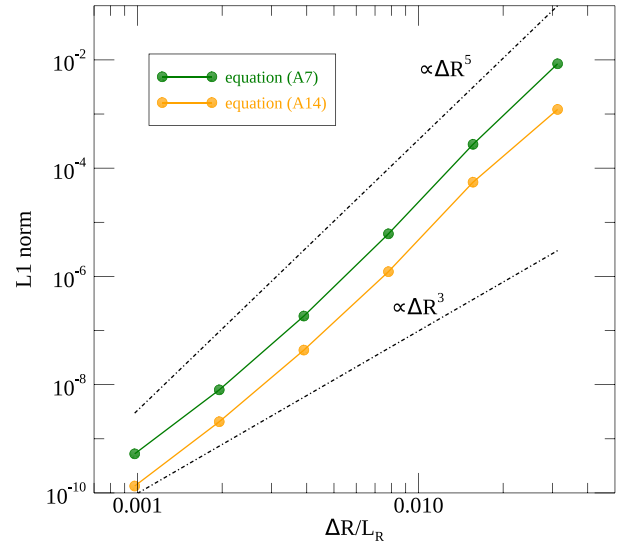


Fig. 16. One-dimensional magnetic confinement of a cylindrical plasma column was examined with various cell sizes. The L_1 norm errors are shown for the normal [equation (A7), green] and volume-weighted [equation (A14), orange] MP5 reconstructions. The dashed lines indicate the orders of accuracy in space. (Color online)

$$V_R = V_z = 0, \quad (\text{A20})$$

$$p = C_{s0}^2 \frac{\rho}{\gamma}, \quad (\text{A21})$$

where $C_{s0} = 4 \times 10^{-3}$ is the sound speed in the ambient medium. Inside the spherical region of $0 \leq \sqrt{R^2 + z^2} \leq 1.0$,

$$\rho V_R R^2 = 1.0 \quad (\text{A22})$$

$$V_R = \tanh\left(\frac{\sqrt{R^2 + z^2}}{0.2}\right) \frac{R}{\sqrt{R^2 + z^2}}, \quad (\text{A23})$$

$$V_z = \tanh\left(\frac{\sqrt{R^2 + z^2}}{0.2}\right) \frac{z}{\sqrt{R^2 + z^2}}, \quad (\text{A24})$$

$$p = \frac{\rho^\gamma C_{s1}^2}{\gamma}, \quad (\text{A25})$$

where $C_{s1} = 3 \times 10^{-2}$ is the sound speed in the wind region. The initial cell-averaged quantities for these configurations were numerically obtained by Simpson's rule. The profiles in the spherical region were set constant in time so a supersonic flow blows out from the inner spherical region. Initialized by this setup, the time evolution was solved in a simulation domain that covered $0 \leq R \leq 10$ and $-10 \leq z \leq 10$ with 256×512 computational cells ($\Delta R = \Delta z = 1.95 \times 10^{-2}$). The open boundary condition was applied at $R = 10.0$ and $|z| = 10.0$.

When using equation (A7) for the reconstruction in the R -direction, the forward shock was subject to a spurious deformation in addition to a trail in the rarefied region

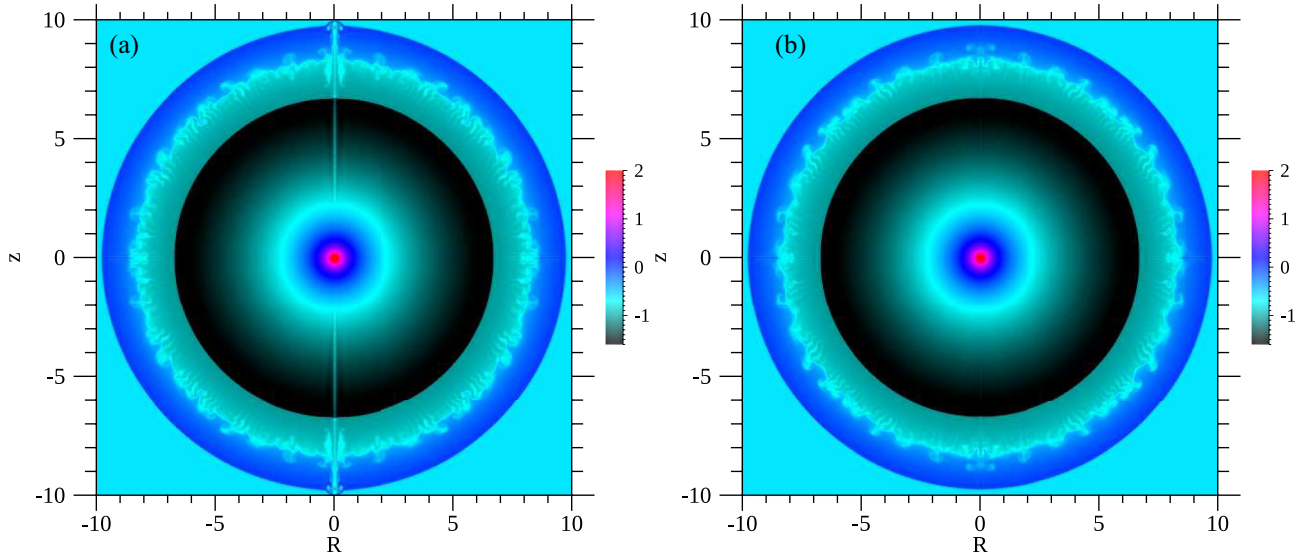


Fig. 17. Blast-wave propagation test in 2D cylindrical coordinates (R, z). Mass density profiles in a logarithmic scale are shown for the reconstruction procedures of (a) equation (A7) and (b) equation (A14). (Color online)

along the z -axis (figure 17a). The growth of the numerical artifacts near the z -axis ceased and the solution was greatly improved (figure 17b) by incorporating the curvature effect of the cell into the reconstruction [equation (A14)]. The turbulent evolution of the Rayleigh–Taylor instability at the contact discontinuity between the sharp shock wave fronts highlights the superior capability of CANS+, which employs the MP5 scheme and the HLLD approximate Riemann solver.

Appendix 3. Accuracy of the resistivity terms

In this section we present a convergence test of the magnetic diffusion problem presented by Matsumoto 2011 to evaluate the source term representation associated with a finite magnetic resistivity [equations (3) and (4)].

The current density $\mathbf{j} = \nabla \times \mathbf{B}$ is evaluated by the second-order central finite difference, for example,

$$j_{x(i,j)} = \frac{\partial B_z}{\partial y} = \frac{B_{z(i,j+1)} - B_{z(i,j-1)}}{2\Delta y}, \quad (\text{A26})$$

where Δy is the cell size in the y -direction and (i, j) indicates the cell number in two dimensions. Then, the current density at the cell surface is obtained by the arithmetic average of the two neighboring cell-center values and is added to the numerical flux F^* of the ideal MHD part,

$$F_{i,j+1/2}^* = F_{i,j+1/2}^* + \frac{\eta_{(i,j)} j_{x(i,j)} + \eta_{(i,j+1)} j_{x(i,j+1)}}{2}. \quad (\text{A27})$$

Here, we only focus on the diffusion term in the induction equation ($F^* = 0$),

$$\frac{\partial \mathbf{B}}{\partial t} = \nabla \times (\eta \mathbf{j}) = \nabla \times (\eta \nabla \times \mathbf{B}). \quad (\text{A28})$$

This equation was solved in a 2D plane for $0 \leq x \leq 1$ and $0 \leq y \leq 0.5$ with the periodic boundary condition in each direction. The z -component of the magnetic field was initially provided by

$$B_z = \sin(\mathbf{k} \cdot \mathbf{r}), \quad (\text{A29})$$

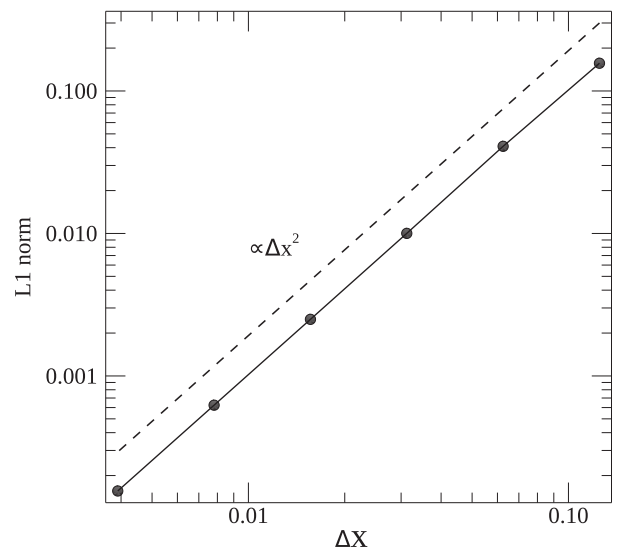


Fig. 18. L_1 norm errors of the magnetic diffusion problem for various cell sizes. The dashed line indicates the second-order accuracy in space.

where $\mathbf{k} = 2\pi(1, 2)^T$ and $\mathbf{r} = (x, y)^T$. The analytic solution to the present diffusion problem can be obtained as

$$B_z(t) = \exp(-\eta|\mathbf{k}^2|t) \sin(\mathbf{k} \cdot \mathbf{r}), \quad (\text{A30})$$

with which L_1 norm errors were calculated at a time of $t = 4 \times 10^{-3}$ with various cell sizes from $\Delta x = \Delta y = 1/8$ to $\Delta x = \Delta y = 1/256$ under a fixed diffusion number of $\sigma_d = 0.3$. We adopted $\eta = 1.0$.

Figure 18 shows the L_1 norm errors as a function of various cell sizes. As expected, the errors decreased as the cell size got smaller, following the second-order accuracy slope. Nevertheless, the resistivity terms become important in localized regions inside current layers (e.g., the magnetic reconnection region shown in sub-subsection 3.2.5), and the impacts of the lower-order representation on the overall spatial accuracy are generally limited.

References

- Asai, N., Fukuda, N., & Matsumoto, R. 2004, *ApJ*, 606, L105
- Brackbill, J. U., & Barnes, D. C. 1980, *J. Comput. Phys.*, 35, 426
- Brio, M., & Wu, C. C. 1988, *J. Comput. Phys.*, 75, 400
- Colella, P., & Woodward, P. R. 1984, *J. Comput. Phys.*, 54, 174
- Dedner, A., Kemm, F., Kröner, D., Munz, C.-D., Schnitzler, T., & Wesenberg, M. 2002, *J. Comput. Phys.*, 175, 645
- Evans, C. R., & Hawley, J. F. 1988, *ApJ*, 332, 659
- Gardiner, T. A., & Stone, J. M. 2005, *J. Comput. Phys.*, 205, 509
- Gottlieb, S., & Shu, C.-W. 1998, *Math. Comput. Am. Math. Soc.*, 67, 73
- Hanayama, H., Takahashi, K., Kotake, K., Oguri, M., Ichiki, K., & Ohno, H. 2005, *ApJ*, 633, 941
- Harten, A., Engquist, B., Osher, S., & Chakravarthy, S. R. 1987, *J. Comput. Phys.*, 71, 231
- Harten, A., Lax, P. D., & van Leer, B. 1983, *SIAM Rev.*, 25, 35
- Hawley, J. F., & Stone, J. M. 1995, *Compt. Phys. Commun.*, 89, 127
- Isobe, H., Miyagoshi, T., Shibata, K., & Yokoyama, T. 2005, *Nature*, 434, 478
- Kritsuk, A. G., et al. 2011, *ApJ*, 737, 13
- Kudoh, T., Matsumoto, R., & Shibata, K. 1999, *ApJ*, 521, 934
- Lee, D. 2013, *J. Comput. Phys.*, 243, 269
- Lee, D., & Deane, A. E. 2009, *J. Comput. Phys.*, 228, 952
- Lee, D., Faller, H., & Reyes, A. 2017, *J. Comput. Phys.*, 341, 230
- Li, S. 2005, *J. Comput. Phys.*, 203, 344
- Londrillo, P., & del Zanna, L. 2004, *J. Comput. Phys.*, 195, 17
- Machida, M., & Matsumoto, R. 2003, *ApJ*, 585, 429
- Machida, M., Nakamura, K. E., Kudoh, T., Akahori, T., Sofue, Y., & Matsumoto, R. 2013, *ApJ*, 764, 81
- Matsumoto, J., Masada, Y., Asano, E., & Shibata, K. 2011, *ApJ*, 733, 18
- Matsumoto, R., Horiuchi, T., Shibata, K., & Hanawa, T. 1988, *PASJ*, 40, 171
- Matsumoto, T. 2011, *PASJ*, 63, 317
- Matsumoto, Y., & Hoshino, M. 2004, *Geophys. Res. Lett.*, 31, L02807
- Matsumoto, Y., & Seki, K. 2010, *JGR*, 115, A10231
- Mignone, A. 2014, *J. Comput. Phys.*, 270, 784
- Mignone, A., Bodo, G., Massaglia, S., Matsakos, T., Tesileanu, O., Zanni, C., & Ferrari, A. 2007, *ApJS*, 170, 228
- Mignone, A., Tzeferacos, P., & Bodo, G. 2010, *J. Comput. Phys.*, 229, 5896
- Minoshima, T., Hirose, S., & Sano, T. 2015, *ApJ*, 808, 54
- Minoshima, T., Miyoshi, T., & Matsumoto, Y. 2019, *ApJS*, 242, 14
- Miyoshi, T., & Kusano, K. 2005, *J. Comput. Phys.*, 208, 315
- Miyoshi, T., & Kusano, K. 2011, *Plasma Fusion Res.*, 6,
- Nishikori, H., Machida, M., & Matsumoto, R. 2006, *ApJ*, 641, 862
- Okada, R., Fukue, J., & Matsumoto, R. 1989, *PASJ*, 41, 133
- Orszag, S. A., & Tang, C.-M. 1979, *J. Fluid Mech.*, 90, 129
- Paczyński, B., & Wiita, P. J. 1980, *A&A*, 88, 23
- Parker, E. N. 1966, *ApJ*, 145, 811
- Powell, K. G., Roe, P. L., Linde, T. J., Gombosi, T. I., & De Zeeuw, D. L. 1999, *J. Comput. Phys.*, 154, 284
- Roe, P. L. 1981, *J. Comput. Phys.*, 43, 357
- Rubin, E. L., & Burstein, S. Z. 1967, *J. Comput. Phys.*, 2, 178
- Ryu, D., & Jones, T. W. 1995, *ApJ*, 442, 228
- Shakura, N. I., & Sunyaev, R. A. 1973, *A&A*, 24, 337
- Shibata, K. 1983, *PASJ*, 35, 263
- Stone, J. M., Gardiner, T. A., Teuben, P., Hawley, J. F., & Simon, J. B. 2008, *ApJS*, 178, 137
- Stone, J. M., Hawley, J. F., Evans, C. R., & Norman, M. L. 1992, *ApJ*, 388, 415
- Stone, J. M., & Pringle, J. E. 2001, *MNRAS*, 322, 461
- Suresh, A., & Huynh, H. T. 1997, *J. Comput. Phys.*, 136, 83
- Takahashi, H. R., & Ohsuga, K. 2013, *ApJ*, 772, 127
- Tao, C., Kataoka, R., Fukunishi, H., Takahashi, Y., & Yokoyama, T. 2005, *JGR*, 110, A11208
- Toriumi, S., & Yokoyama, T. 2011, *ApJ*, 735, 126
- Tóth, G. 2000, *J. Comput. Phys.*, 161, 605
- Tsubouchi, K. 2009, *JGR*, 114, A02101
- van Leer, B. 1979, *J. Comput. Phys.*, 32, 101
- Yabe, T., Xiao, F., & Utsumi, T. 2001, *J. Comput. Phys.*, 169, 556
- Zenitani, S. 2015, *Phys. Plasmas*, 22, 032114
- Zenitani, S., & Miyoshi, T. 2011, *Phys. Plasmas*, 18, 022105